A Series-Connected 40-Pulse Rectifier With DC Link Passive Harmonic Reduction Circuit

Qingxiao Du, Wei Liu, Quanhui Li, Lei Gao, and Fangang Meng, *Member, IEEE*

***Abstract*—This article is focused on power quality improvement of the series-connected multipulse rectifiers (MPRs). For the dc side passive harmonic reduction method, the optimum design of the harmonic injection transformer is the key point to achieve the optimal harmonic elimination effect. First, a novel method for determining the optimum turns ratio of the harmonic injection transformer is proposed. Then, in combination with a five-phase bridge-rectifier-based MPR, the correctness of the general calculation formula is verified. In the verification processes, the operation principle and harmonic reduction mechanism are clearly analyzed before and after using the harmonic reduction circuit (HRC). The optimum turns ratio of the harmonic injection transformer obtained from the view point of minimizing the input voltage total harmonic distortion (THD) value is consistent with that calculated from general formula. Under the optimum design, the kVA rating of the HRC is only 0.87% of the load power. In experimental, the THD values of the input voltages in the 20-pulse rectifier and 40-pulse rectifier are 3.32% and 2.07%, respectively. The proposed method greatly reduces the complexity of the design processes and helpful for the development of the super-MPR. The proposed 40-pulse rectifier has high reliability, easy realization, considerable harmonic reduction ability, and quite a low load voltage ripple coefficient.**

***Index Terms*—Five-phase diode bridge rectifier, harmonic injection transformer, optimum turns ratio design, power quality, series-connected multipulse rectifier (MPR).**

I. Introduction

In order to deal with harmonic pollutions caused by the strong nonlinearity of rectification devices, some useful methods have been proposed [1]–[3]. In recent decades, the method of modifying rectifiers themselves has experienced a rapid development stage with the gradual maturity of PWM technology and multipulse rectification technology. Compared with PWM rectifiers, multipulse rectifiers (MPRs) based on diode bridge rectifiers have advantages of easy realization, high reliability, better overload capacity, and lower overall cost, so that they are more suitable for high power occasions [4], [5].

Manuscript received August 20, 2020; revised December 21, 2020, May 9, 2021, and July 29, 2021; accepted September 5, 2021. Date of publication September 8, 2021; date of current version November 30, 2021. This work was supported in part by the National Natural Foundation of China under Grant 51777042 and in part by the Natural Foundation of Shandong Province under Grant ZR2020ME199. Recommended for publication by Associate Editor J. C. Clare. *(Corresponding author: Fangang Meng.)*

The authors are with the School of Electrical Engineering and Automation, Harbin Institute of Technology, Harbin 150001, China (e-mail: 690384469@qq.com; l61847@163.com; a875921420@qq.com; hualeier111@126.com; mfg0327@sina.com).

Color versions of one or more figures in this article are available at https://doi.org/10.1109/TPEL.2021.3110976.

Digital Object Identifier 10.1109/TPEL.2021.3110976

Compared to parallel-connected MPRs, series-connected MPRs are more suitable for high voltage or high-power occasions, such as high-voltage dc transmission, high-power frequency conversion speed regulation, and large-capacity battery charging, etc. For improving their harmonic reduction abilities, some useful dc side harmonic reduction methods of MPRs have been proposed. Since the phase-shifting transformer design for a 12-pulse rectifier is more conventional. Therefore, dc side harmonic reduction circuit (HRC) design is usually based on a 12-pulse rectifier [6], [7].

For parallel-connected MPRs, reducing total kVA rating of magnetic devices in a rectification system is considered as an important research direction just as improving power quality on both ac and dc sides. Many kinds of autotransformers have been proposed to replace isolate transformer in some occasions do not need electrical isolation, such as star-connected autotransformer [8], zigzag configured autotransformer [9], and delta-connected autotransformer [10]. When combining conventional 12-pulse rectifiers with dc side dual passive HRCs, parallel-connected 36-pulse rectifiers can be formed [8]–[10]. However, autotransformer is not suitable for series-connected MPRs, only half-isolated transformers [11]–[15] or full-isolated transformers [16], [17] have been verified to match with series-connected MPRs.

In [11] and [12], two kinds of series-connected 24-pulse rectifiers with a single passive HRC are proposed. Accordingly, for further reducing harmonics, two kinds of 36-pulse rectifier with dc side dual-passive HRCs are proposed in [13] and [14]. Based on [13], a bidirectional switch is added to dc side HRC, so that a 48-pulse rectifier is formed [15]. The phase-shifting transformers in these five topologies are all half-isolated transformer, in order to provide a full isolation solution for occasions that need electrical isolation, a series-connected 24-pulse based on a $\Delta/\Delta/Y$ transformer is proposed in [16], whose HRC is only consisted with a single-phase transformer and a single-phase full-wave rectifier. In [17], a 30-pulse rectifier is constructed, which contains three series-connected three-phase diode bridge rectifiers in the main circuit, two sets of HRCs have to be added to increase pulse numbers. These papers indicate that it is a useful way to achieve a better harmonic reduction effect under normal operation conditions by using more three-phase bridge rectifiers in the main circuit and more suitable HRCs in the auxiliary circuit.

In the performance improvement aspect, fault tolerance ability is another important criterion to do comprehensive evaluations on MPRs except for total harmonic distortion (THD) values. It

can be observed that each diode in three-phase bridge rectifiers conducts 120° per power cycle [16], [17]. And each operation mode corresponds to a specific interval of input currents, if a diode in the main circuit is under open-circuit fault conditions, the affected interval length of input currents is around 120° for a three-phase rectifier based MPR. For a five-phase based MPR, the conduction angle of each diode in the main circuit decreases to 72° per cycle, the power quality can be kept in a better state under diode open-circuit fault conditions. Therefore, as the phase number of the bridge rectifier in the main circuit increases, the fault tolerance of the system can be improved to a certain extent. At the same time, the design processes for the main transformer will be more complex. It needs to give full consideration to reliability and complexity for a specific MPR design, so that this article takes a 20-pulse rectifier as a basic circuit to design its transformer and auxiliary circuit. In [18] and [19], the five-phase bridge rectifiers are used in parallel-connected MPRs. Due to the derivation process of operation modes for parallel-connected MPRs, harmonic reduction mechanism and design principle of dc side HRC are all different from that in series-connected MPRs, it also has research values in series-connected MPRs.

For [11]–[15], the use of a half-isolated main transformer makes it easier to establish current relations flowing through each phase of the transformer, similarly, the current source model is also considered suitable for a full isolated transformer with six output phases as shown in [16] and [17]. However, with increasing the output phase number of the phase-shifting transformer, the current waveform flowing through each phase of the rectifiers cannot be directly plotted especially for a full-isolated main transformer. It is necessary to find a more convenient method to do HRC design. Moreover, compared to [17], in our design, the pulse number increases through increasing phase number in each bridge rectifier, the HRC needs to be designed once only.

This article proposes a new method for determining the optimum turns ratio of the single-phase transformer in the passive HRC. This method is quite different from the previous references, and it is adaptable for the 8*N*-pulse (*N* is any odd number greater than or equal to three) series-connected MPRs with the same harmonic reduction method. The general calculation formula for the optimum turns ratio is derived, in combination with the original method, the correctness of the new method is verified. The passive harmonic reduction mechanism and HRC design principles are also analyzed in detail for a basic 20-pulse rectifier, which helps readers to comprehensively understand operation modes of series-connected MPRs and gives an essential theoretical guidance for other HRC design. Besides, related simulation and experimental results are also presented to verify the effectiveness of the proposed MPR.

II. Novel Optimum Turns Ratio Design Method for the Harmonic Injection Transformer

Fig. 1 is the 8*N*-pulse series-connected MPR with dc side passive HRC, in the main circuit, two *N*-phase diode bridge rectifiers are connected in series; the HRC contains a single-phase transformer and a single-phase diode bridge/full-wave rectifier.

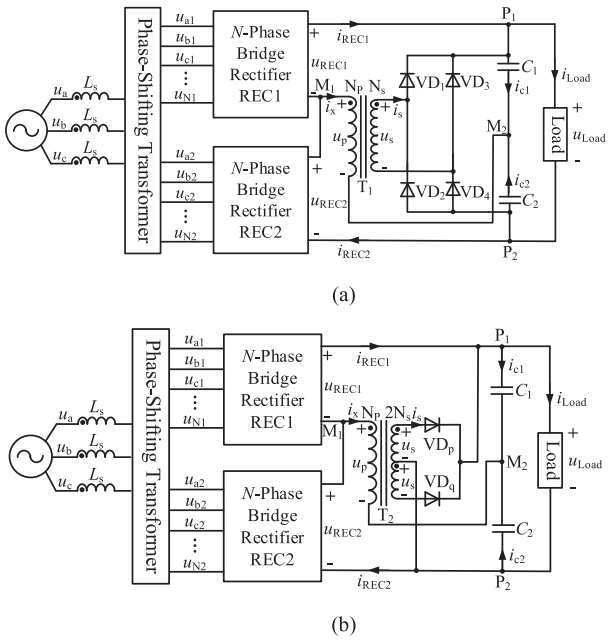

Fig. 1. Current source series-connected 8*N*-pulse rectifier. (a) With single-phase diode bridge rectifier. (b) With single-phase full-wave rectifier.

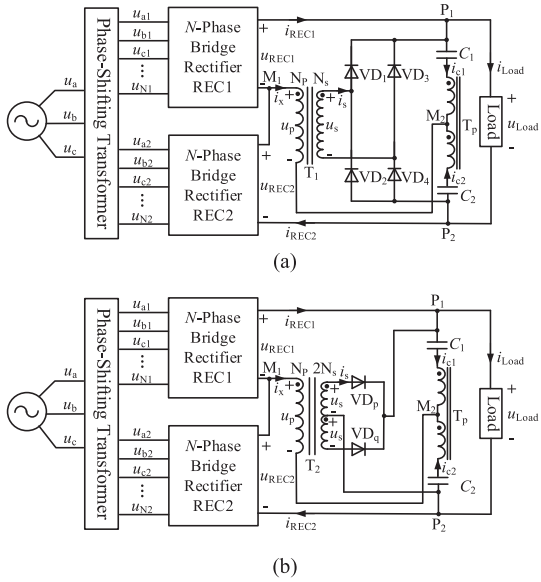

Fig. 2. Voltage source series-connected 8*N*-pulse rectifier. (a) With single-phase diode bridge rectifier. (b) With single-phase full-wave rectifier.

In this HRC, the optimum design of the single-phase transformer is the key point to achieve the optimal harmonic elimination effect. In theoretical analysis processes, in order to establish the relations between the turns ratio of transformer T_1/T_2 and the input current or the load voltage, the current source rectifier is replaced by the voltage source rectifier as shown in Fig. 2. These two rectifiers have the same operation mode and harmonic reduction method, so that the optimum turns ratio should have a certain correlation.

First, based on Fig. 2, the general calculation formula for the optimum turns ratio of the single-phase transformer (T_1) connected with the bridge rectifier is derived.

Assume that the three-phase input voltages are

$$\begin{cases} u_{\mathrm{a}} = \sqrt{2}E\sin\omega t \\ u_{\mathrm{b}} = \sqrt{2}E\sin(\omega t - 2\pi/3) \\ u_{\mathrm{c}} = \sqrt{2}E\sin(\omega t + 2\pi/3) \end{cases} \tag{1}$$

where E is the rms value of the input voltages.

The output voltages of the phase-shifting transformer are

$$\begin{cases} u_{\mathrm{a1}} = \sqrt{2}KE\sin\omega t \\ u_{\mathrm{b1}} = \sqrt{2}KE\sin(\omega t - 2\pi/N) \\ u_{\mathrm{c1}} = \sqrt{2}KE\sin(\omega t - 4\pi/N) \\ \vdots \\ u_{(\mathrm{N}-1)1} = \sqrt{2}KE\sin(\omega t + 4\pi/N) \\ u_{\mathrm{N1}} = \sqrt{2}KE\sin(\omega t + 2\pi/N) \end{cases}$$

$$\begin{cases} u_{\mathrm{a2}} = \sqrt{2}KE\sin(\omega t + \pi/2N) \\ u_{\mathrm{b2}} = \sqrt{2}KE\sin(\omega t - 3\pi/2N) \\ u_{\mathrm{c2}} = \sqrt{2}KE\sin(\omega t - 7\pi/2N) \\ \vdots \\ u_{(\mathrm{N}-1)2} = \sqrt{2}KE\sin(\omega t + 9\pi/2N) \\ u_{\mathrm{N2}} = \sqrt{2}KE\sin(\omega t + 5\pi/2N) \end{cases} \tag{2}$$

where K is the ratio of the input to output rms voltage of the phase-shifting transformer, and N is the phase number of the diode bridge rectifier in the main circuit.

The turns ratio of the transformer T_1 is

$$m = \frac{u_{\mathrm{s}}}{u_{\mathrm{p}}} = \frac{N_{\mathrm{s}}}{N_{\mathrm{p}}}. \tag{3}$$

In Fig. 2, according to the KVL, regardless of whether the HRC works, the rectifier always has the following relationship:

$$\begin{cases} u_{\mathrm{REC1}} = u_{\mathrm{P1M2}} - u_{\mathrm{p}} \\ u_{\mathrm{REC2}} = u_{\mathrm{M2P2}} + u_{\mathrm{p}} \\ u_{\mathrm{P1M2}} = u_{\mathrm{M2P2}} = \frac{u_{\mathrm{Load}}}{2} \end{cases} \Rightarrow \begin{cases} u_{\mathrm{p}} = \frac{u_{\mathrm{REC2}} - u_{\mathrm{REC1}}}{2} \\ u_{\mathrm{Load}} = u_{\mathrm{REC1}} + u_{\mathrm{REC2}}. \end{cases} \tag{4}$$

When without using the HRC, the rectifier operates in the 4N-pulse rectification state. The output voltages of the two bridge rectifiers and the load voltages are

$$\begin{cases} u_{\mathrm{REC1\_4N}} = S_{\mathrm{a1}}u_{\mathrm{a1}} + S_{\mathrm{b1}}u_{\mathrm{b1}} + S_{\mathrm{c1}}u_{\mathrm{c1}} + S_{\mathrm{d1}}u_{\mathrm{d1}} + S_{\mathrm{e1}}u_{\mathrm{e1}} \\ u_{\mathrm{REC2\_4N}} = S_{\mathrm{a2}}u_{\mathrm{a2}} + S_{\mathrm{b2}}u_{\mathrm{b2}} + S_{\mathrm{c2}}u_{\mathrm{c2}} + S_{\mathrm{d2}}u_{\mathrm{d2}} + S_{\mathrm{e2}}u_{\mathrm{e2}} \\ u_{\mathrm{Load\_4N}} = u_{\mathrm{REC1\_4N}} + u_{\mathrm{REC2\_4N}} \end{cases} \tag{5}$$

where S_{a1}, S_{b1}, S_{c1}, S_{d1}, S_{e1}, S_{a2}, S_{b2}, S_{c2}, S_{d2}, and S_{e2} are the switching functions of the corresponding phases.

Based on the relations between the voltages u_{s} and u_{load}, there are three operation modes of the HRC.

Mode 1: When $u_{\mathrm{s}} < u_{\mathrm{Load}}$, the HRC is not working.

The output voltages of rectifiers REC1, REC2, and the load voltage are

$$\begin{cases} u_{\mathrm{REC1\_8N}} = u_{\mathrm{REC1\_4N}} \\ u_{\mathrm{REC2\_8N}} = u_{\mathrm{REC2\_4N}} \\ u_{\mathrm{Load\_8N}} = u_{\mathrm{Load\_4N}}. \end{cases} \tag{6}$$

Mode 2: When $u_{\mathrm{s}} > u_{\mathrm{Load}}$, the diodes VD_1 and VD_4 are turned ON, the bridge rectifier REC1 is working and the bridge rectifier REC2 is not working.

Under this operating mode

$$u_{\mathrm{s\_8N}} = mu_{\mathrm{p\_8N}} = u_{\mathrm{Load\_8N}}. \tag{7}$$

In combination with (4) and (7), the following relations can be obtained:

$$\begin{cases} u_{\mathrm{REC1\_8N}} = \frac{m-2}{m+2}u_{\mathrm{REC2\_4N}} \\ u_{\mathrm{REC2\_8N}} = u_{\mathrm{REC2\_4N}} \\ u_{\mathrm{p\_8N}} = \frac{2}{m+2}u_{\mathrm{REC2\_4N}} \\ u_{\mathrm{Load\_8N}} = \frac{2m}{m+2}u_{\mathrm{REC2\_4N}}. \end{cases} \tag{8}$$

Mode 3: When $-u_s > u_{\mathrm{Load}}$, the diodes VD_2 and VD_3 are turned ON, the bridge rectifier REC2 is working and the bridge rectifier REC1 is not working.

Under this operating mode

$$u_{\mathrm{s\_8N}} = mu_{\mathrm{p\_8N}} = -u_{\mathrm{Load\_8N}}. \tag{9}$$

In combination with (4) and (9), the following relations can be obtained:

$$\begin{cases} u_{\mathrm{REC1\_8N}} = u_{\mathrm{REC1\_4N}} \\ u_{\mathrm{REC2\_8N}} = \frac{m-2}{m+2}u_{\mathrm{REC1\_4N}} \\ u_{\mathrm{p\_8N}} = -\frac{2}{m+2}u_{\mathrm{REC1\_4N}} \\ u_{\mathrm{Load\_8N}} = \frac{2m}{m+2}u_{\mathrm{REC1\_4N}}. \end{cases} \tag{10}$$

Ignoring the amplitude $\sqrt{2}\mathrm{KE}$ in (1), the voltages $u_{\mathrm{REC1\_4N}}$ and $u_{\mathrm{REC2\_4N}}$ are

$$u_{\mathrm{REC1\_4N}} = \begin{cases} A\sin(\omega t + \frac{\pi}{2} - \frac{k\pi}{N})\omega t \in \left[\frac{k\pi}{N}, \frac{\pi}{2N} + \frac{k\pi}{N}\right) \\ A\sin(\omega t + \frac{\pi}{2} - \frac{(k+1)\pi}{N})\omega t \in \left[\frac{\pi}{2N} + \frac{k\pi}{N}, \frac{(k+1)\pi}{N}\right) \end{cases} \tag{11}$$

$$u_{\mathrm{REC2\_4N}} = A\sin\left(\omega t + \frac{\pi}{2} - \frac{\pi}{2N} - \frac{k\pi}{N}\right)\omega t \in \left[\frac{k\pi}{N}, \frac{(k+1)\pi}{N}\right) \tag{12}$$

where A is the coefficient associated with the phase number N, and k is the nature number.

The voltages $u_{\mathrm{p\_4N}}$ and $u_{\mathrm{Load\_4N}}$ are

$$u_{\mathrm{p\_4N}}=\begin{cases}-\frac{A}{2}\sqrt{2-2\cos\frac{\pi}{2N}}\cos(\omega t+\arctan\frac{\sin\frac{\pi}{2N}}{1-\cos\frac{\pi}{2N}}-\frac{k\pi}{N}) \\ \qquad\qquad \omega t\in\left[\frac{k\pi}{N},\ \frac{\pi}{2N}+\frac{k\pi}{N}\right) \\ -\frac{A}{2}\sqrt{2-2\cos\frac{\pi}{2N}}\sin(\omega t-\frac{3\pi}{4N}-\frac{k\pi}{N}) \\ \qquad\qquad \omega t\in\left[\frac{\pi}{2N}+\frac{k\pi}{N},\ \frac{(k+1)\pi}{N}\right)\end{cases} \tag{13}$$

$$u_{\mathrm{Load\_4N}}=A\sqrt{2+2\cos\frac{\pi}{2N}}\sin(\omega t+\arctan\frac{1+\cos\frac{\pi}{2N}}{\sin\frac{\pi}{2N}}-\frac{k\pi}{2N}) \qquad \omega t\in\left[\frac{k\pi}{2N},\ \frac{(k+1)\pi}{2N}\right) \tag{14}$$

where ωt_1 is the first intersection point of the voltages $u_{\mathrm{p\_4N}}$ and $u_{\mathrm{Load\_4N}}$.

In combination with the above analysis, the load voltage $u_{\mathrm{Load\_8N}}$ is

$$u_{\mathrm{Load\_8N}}=\begin{cases}\frac{2m}{m+2}A\sin(\omega t+\frac{\pi}{2}-\frac{k\pi}{2N}) \\ \qquad\qquad \omega t\in\left[\frac{k\pi}{2N},\omega t_1+\frac{k\pi}{2N}\right) \\ A\sqrt{2+2\cos\frac{\pi}{2N}}\sin\left[\omega t+\arctan(\frac{1+\cos\frac{\pi}{2N}}{\sin\frac{\pi}{2N}})-\frac{k\pi}{2N}\right] \\ \qquad\qquad \omega t\in\left[\omega t_1+\frac{k\pi}{2N},-\omega t_1+\frac{(k+1)\pi}{2N}\right) \\ \frac{2m}{m+2}A\sin(\omega t+\frac{\pi}{2}-\frac{(k+1)\pi}{2N}) \\ \qquad\qquad \omega t\in\left[-\omega t_1+\frac{(k+1)\pi}{2N},\frac{(k+1)\pi}{2N}\right).\end{cases} \tag{15}$$

From (15), it can be observed that the turns ratio m is associated with the amplitude of the load voltage. From the viewpoint of minimizing the ripple factor of the load voltage, the amplitude of the piecewise function should be the same.

Therefore, the turns ratio m is

$$m=\frac{2\sqrt{2+2\cos\frac{\pi}{2N}}}{2-\sqrt{2+2\cos\frac{\pi}{2N}}}. \tag{16}$$

If the rectifier in the HRC is the single-phase full-wave rectifier as shown in Figs. 1(b) and 2(b), there are half of the secondary windings connected into the circuit when the HRC is working. Defining that the turns ratio of the single-phase transformer T_2 still fulfills (2), the optimum turns ratio m is consistent with that for the HRC with single-phase diode bridge rectifier [see Figs. 1(a) and 2(a)]. The general calculation formula (16) is suitable for the two kinds of HRC.

Substitute $N=5$ into (16), m takes 160.45 in theory. In this section, the optimum turns ratio design for the current source rectifier is translated into that in the voltage source rectifier, then the derivation is presented from minimizing the load ripple factor. In real design, the current source rectifier is more attractive due to it can supply high quality power on both ac and dc sides. To verify the correctness of the novel design method proposed in Section II, the passive HRC is designed by using the conventional method based on a current-source series-connected 20-pulse rectifier in the following sections.

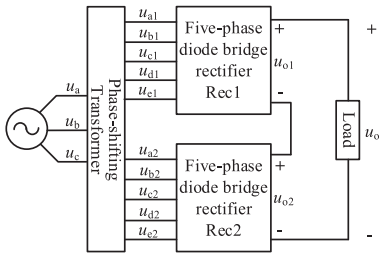

Fig. 3. Configuration of the series-connected 20-pulse rectifier.

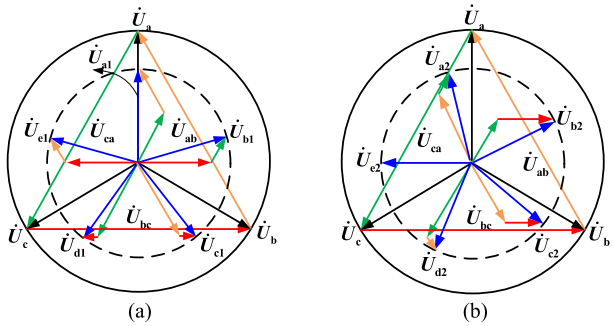

Fig. 4. Phasor diagram of the phase-shifting transformer. (a) Phasor diagram of the first set of output voltages. (b) Phasor diagram of the second set of output voltages.

III. Phase-Shifting Transformer Design

Fig. 3 is the configuration of the series-connected 20-pulse rectifier, in which, Rec1 and Rec2 are two sets of five-phase series-connected diode bridge rectifiers.

Based on the rectification principle, in order to make sure that all diode bridge rectifiers in the main circuit of MPR can operate normally, the phase difference θ between several sets of output voltages provided by the phase-shifting transformer fulfills

$$\theta=\frac{360^{\mathrm{o}}}{N_1N_2} \tag{17}$$

where N_1 is the number of output pulses of each bridge rectifier and N_2 is the number of bridge rectifiers.

In combination with Fig. 3 and (17), the two sets of five-phase output voltages should meet the following conditions: they have the same rms value, and the phase difference is 18°. In order to improve the safety of the rectifier, a completely isolated phase-shifting transformer is designed, the primary windings are in delta-connection, the secondary side windings are in two sets of zigzag-connection. Assuming that the ratio of the rms value of the input and output phase voltages is K ($K\geq 1$), the phasor diagram of the phase-shifting transformer is shown in Fig. 4. In Fig. 4, the phasors $\dot{\mathrm{U}}$a, $\dot{\mathrm{U}}$b, and $\dot{\mathrm{U}}$c correspond to the input voltages of phase "a," phase "b," and phase "c," with a phase difference of 120°; phasors $\dot{\mathrm{U}}$a1 , $\dot{\mathrm{U}}$b1, $\dot{\mathrm{U}}$c1, $\dot{\mathrm{U}}$d1, and $\dot{\mathrm{U}}$e1 are the first set of five-phase output voltages with a phase difference of 72°; phasors $\dot{\mathrm{U}}$a2, $\dot{\mathrm{U}}$b2, $\dot{\mathrm{U}}$c2, $\dot{\mathrm{U}}$d2, and $\dot{\mathrm{U}}$e2 are the second

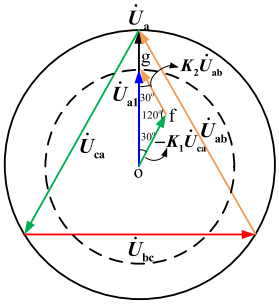

Fig. 5. Phasor synthesis schematic of phasor $\dot{U}a$.

set of five-phase output voltages, which respectively lags behind the phasor $\dot{U}a1$, $\dot{U}b1$, $\dot{U}c1$, $\dot{U}d1$, and $\dot{U}e1$ 18°.

In this part, taking phasor $\dot{U}a$ as an example to clarify the specific synthetic process. Fig. 5 shows the phasor synthesis schematic of phasor $\dot{U}a$.

On the basis of phasors $\dot{U}ab$, $\dot{U}bc$, and $\dot{U}ca$, in Fig. 5, the phasor $\dot{U}a$ can be presented as

$$\dot{U}_{a1} = -K_1 \dot{U}_{ca} + K_2 \dot{U}_{ab} \tag{18}$$

where K_1 and K_2 are the proportional coefficients of the secondary winding relative to the primary winding.

In the Δ**ofg** as shown in Fig. 5, according to the Law of Sines, the following relationship exists between the rms value of each phasor:

$$\frac{U_{a1}}{\sin 120^\circ} = \frac{K_1 U_{ca}}{\sin 30^\circ} = \frac{K_2 U_{ab}}{\sin 30^\circ} \tag{19}$$

where U_{a1}, U_{ca}, and U_{ab} are the rms values of phasor $\dot{U}a1$, $\dot{U}ca$, and $\dot{U}ab$, respectively.

It can be observed from Fig. 4 that

$$U_{ab} = U_{ca} = \sqrt{3} K U_{a1}. \tag{20}$$

Substitute (20) into (19), the proportional coefficients K_1 and K_2 can be calculated out

$$K_1 = K_2 = \frac{\sin 30^\circ}{\sqrt{3} K \sin 120^\circ}. \tag{21}$$

Fig. 6 shows the winding configuration of the phase-shifting transformer with delta-double zigzag connection, in which the turns number of each winding is represented by N plus the number subscript. When the primary windings "a," "b," and "c" are respectively coiled on the A-, B-, and C-phase core columns of the transformer, the A-phase secondary winding "a1" and the C-phase secondary winding "c1" is connected together to synthesize the phasor $\dot{U}a1$. Based on the above analysis, the winding structure of the remaining phases can be obtained in the same way.

It is known that the ratio of the rms value of each phasor is equal to turns ratio of the corresponding transformer windings, so that the relationship between the turns number of the primary and secondary windings on the A-, B-, and C-phase core columns fulfills (62) in the Appendix.

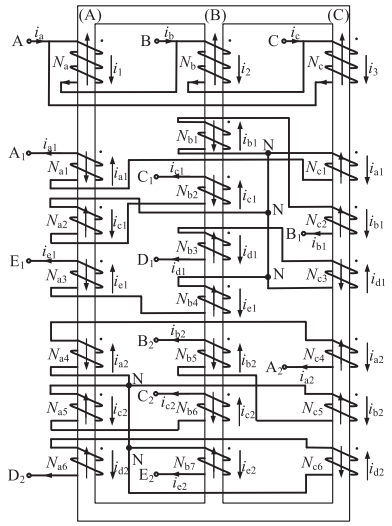

Fig. 6. Winding configuration of the phase-shifting transformer.

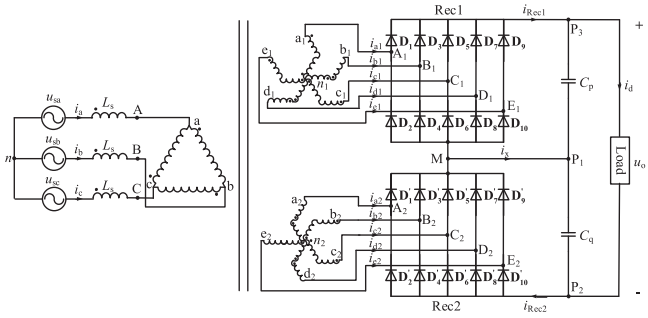

Fig. 7. Proposed series-connected 20-pulse rectifier.

IV. Accuracy Verification of the Equivalent Current Source Model for the Proposed 20-Pulse Rectifier

In order to verify the accuracy of the equivalent current source model in the 20-pulse rectifier and provide the theoretical basis of the research on the dc side harmonic reduction method, a series-connected 20-pulse rectifier based on five-phase bridge rectifiers is proposed as shown in Fig. 7. In Fig. 7, the phase-shifting transformer is the isolation transformer designed in Section III. The ac side three-phase voltage sources are connected in series with three inductors L_s, and the dc side load is connected in parallel with two large capacitors with same capacitance values, so that this rectifier can be regarded as a current source rectifier with constant voltage load.

A. Operation Modes Analysis of the 20-Pulse Rectifier

Since this rectifier is a current source rectifier, the ac side input current waveforms can be seen as sine waves, while the primary and secondary side voltage waveforms of the phase-shifting transformer are unknown. Theoretically, the operation modes of the rectifier should be determined by the current relationship. Combining Fig. 6 with the principle of Ampere-turns balance, it can be found that the process of establishing the current

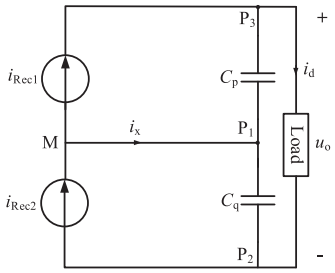

Fig. 8. Equivalent current source model of the proposed 20-pulse rectifier.

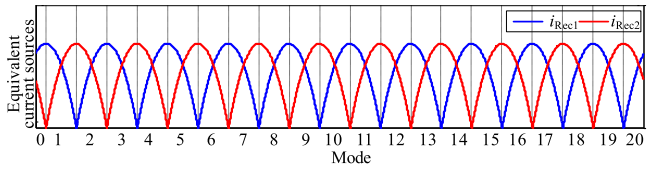

Fig. 9. Equivalent current source waveforms.

relationship between the primary and secondary windings of this phase-shifting transformer is quite complicated; and the secondary current waveforms cannot be directly determined by the primary currents, but the phase relationship of the secondary currents can be determined by the phase shift angle of the transformer. Therefore, the equivalent current source model shown in Fig. 8 is proposed, assuming that it is adapted to the rectifier shown in Fig. 7.

In Fig. 8, the bridge rectifiers Rec1 and Rec2 are equivalent to two current sources i_{Rec1} and i_{Rec2} with the same rms value and a phase difference of 18°. The connection of midpoints M and P_1 can provide a circulation loop for the instantaneous current difference i_{x} between i_{Rec1} and i_{Rec2}.

After using the ac side inductors, the waveforms of the equivalent current sources i_{Rec1} and i_{Rec2} are shown in Fig. 9, where φ is the phase difference of the AC side phase currents (i_{a}, i_{b}, i_{c}) lagging behind the ac voltage sources (u_{sa}, u_{sb}, u_{sc}). In Fig. 9, the interval of each mode and the values of current sources i_{Rec1} and i_{Rec2} in each interval are shown in Table I. According to the values of i_{Rec1} and i_{Rec2}, the conduction mode of the diodes in the two five-phase bridge rectifiers can be obtained. It can be seen from Table I that each diode is turned on for 72° per power cycle, and at any moment, there is a conductive diode on the upper and lower bridge arms of each rectifier.

B. Formation Process of the Input Voltage $u_{An,20}$

Combining Table II with Kirchhoff's Voltage Law (KVL), the ac side voltage value corresponding to each interval can be determined. Taking Mode 1 as an example to calculate the expression of voltage $u_{\mathrm{An},20}$ in interval [φ, φ+18°).

In Fig. 7, P_1 and P_2 are defined as reference points of rectifiers Rec1 and Rec2, respectively. To facilitate analysis, assuming that the proportional coefficient K is equal to 1, so that the input voltage u_{An} and the output voltage u_{A1n1} of the transformer both

TABLE I
DIODE CONDUCTION MODE OF THE SERIES-CONNECTED 20-PULSE RECTIFIER

Mode	Interval	i_{Rec1}	i_{Rec2}	Conductive Diodes
0	[0, φ)	i_{e1b1}	i_{e2b2}	D_4 D_9 D_4' D_9'
1	[φ, φ+18°)	i_{e1b1}	i_{e2c2}	D_4 D_9 D_6' D_9'
2	[φ+18°, φ+36°)	i_{e1c1}	i_{e2c2}	D_6 D_9 D_6' D_9'
3	[φ+36°, φ+54°)	i_{e1c1}	i_{a2c2}	D_6 D_9 D_1' D_6'
4	[φ+54°, φ+72°)	i_{a1c1}	i_{a2c2}	D_1 D_6 D_1' D_6'
5	[φ+72°, φ+90°)	i_{a1c1}	i_{a2d2}	D_1 D_6 D_1' D_8'
6	[φ+90°, φ+108°)	i_{a1d1}	i_{a2d2}	D_1 D_8 D_1' D_8'
7	[φ+108°, φ+126°)	i_{a1d1}	i_{b2d2}	D_1 D_8 D_3' D_8'
8	[φ+126°, φ+144°)	i_{b1d1}	i_{b2d2}	D_3 D_8 D_3' D_8'
9	[φ+144°, φ+162°)	i_{b1d1}	i_{b2e2}	D_3 D_8 D_3' D_{10}'
10	[φ+162°, φ+180°)	i_{b1e1}	i_{b2e2}	D_3 D_{10} D_3' D_{10}'
11	[φ+180°, φ+198°)	i_{b1e1}	i_{c2e2}	D_3 D_{10} D_5' D_{10}'
12	[φ+198°, φ+216)	i_{c1e1}	i_{c2e2}	D_5 D_{10} D_5' D_{10}'
13	[φ+216°, φ+234°)	i_{c1e1}	i_{c2a2}	D_5 D_{10} D_2' D_5'
14	[φ+234°, φ+252°)	i_{c1a1}	i_{c2a2}	D_2 D_6 D_2' D_5'
15	[φ+252°, φ+270°)	i_{c1a1}	i_{d2a2}	D_2 D_6 D_2' D_7'
16	[φ+270°, φ+288°)	i_{d1a1}	i_{d2a2}	D_2 D_8 D_2' D_7'
17	[φ+288°, φ+306°)	i_{d1a1}	i_{d2b2}	D_2 D_8 D_4' D_7'
18	[φ+306°, φ+324°)	i_{d1b1}	i_{d2b2}	D_4 D_8 D_4' D_7'
19	[φ+324°, φ+342°)	i_{d1b1}	i_{e2b2}	D_4 D_8 D_4' D_9'
20	[φ+342°, 360°]	i_{e1b1}	i_{e2b2}	D_4 D_9 D_4' D_9'

TABLE II
LEVEL VALUES OF THE INPUT VOLTAGE $u_{\mathrm{An},20}$

Mode	Level Value	Mode	Level Value
1, 10	$L_1=(\frac{4-5k_1}{10k_2}+\frac{1}{5k_1}-\frac{1}{2})(u_o+4U_d)$	11, 20, 0	$-L_1$
2, 9	$L_2=(\frac{-1+5k_1}{10k_2}-\frac{3}{10k_1}+\frac{1}{2})(u_o+4U_d)$	12, 19	$-L_2$
3, 8	$L_3=(\frac{3}{10k_1}+\frac{1}{10k_2}-\frac{1}{2})(u_o+4U_d)$	13, 18	$-L_3$
4, 7	$L_4=(-\frac{1}{5k_1}+\frac{1}{10k_2}+\frac{1}{2})(u_o+4U_d)$	14, 17	$-L_4$
5, 6	$L_5=(\frac{1}{5k_1}-\frac{1}{10k_2})(u_o+4U_d)$	15, 16	$-L_5$

can be expressed as

$$u_{\mathrm{An}} = u_{\mathrm{A1n1}} = u_{\mathrm{A1P1}} - u_{\mathrm{n1P1}} = u_{\mathrm{A1P1}} - \frac{u_{\mathrm{A1P1}} + u_{\mathrm{B1P1}} + u_{\mathrm{C1P1}} + u_{\mathrm{D1P1}} + u_{\mathrm{E1P1}}}{5}. \tag{22}$$

Due to the voltage division function of the dc side capacitors, terminal voltage of each capacitor accounts for one-half of the

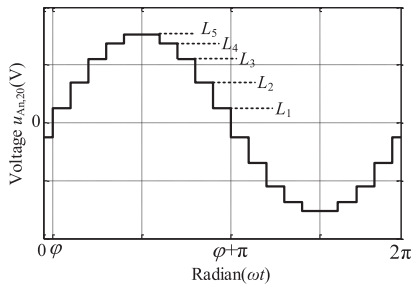

Fig. 10. Waveform of the input voltage $u_{\mathrm{An},20}$.

load voltage. According to KVL and Table II, in the interval [φ, φ+18°), it can be obtained that

$$\begin{cases} u_{\mathrm{E1P1}} = U_{\mathrm{d}} + \frac{u_{\mathrm{o}}}{2} \\ u_{\mathrm{B1P1}} = -U_{\mathrm{d}} \end{cases} \begin{cases} u_{\mathrm{E2P2}} = U_{\mathrm{d}} + \frac{u_{\mathrm{o}}}{2} \\ u_{\mathrm{C2P2}} = -U_{\mathrm{d}} \end{cases} \tag{23}$$

where U_{d} is the forward voltage drop of the diode and u_{o} is the load voltage.

From (23), the voltage u_{E2C2} is

$$u_{\mathrm{E2C2}} = u_{\mathrm{E2P2}} - u_{\mathrm{C2P2}} = 2U_{\mathrm{d}} + \frac{u_{\mathrm{o}}}{2}. \tag{24}$$

In combination with the configuration and turns ratio of the transformer, the voltage u_{E2C2} can also be expressed as

$$\begin{aligned} u_{\mathrm{E2C2}} &= u_{\mathrm{E2n2}} - u_{\mathrm{C2n2}} \\ &= k_1 u_{\mathrm{E1B1}} - k_2 u_{\mathrm{B1A1}} \\ &= k_1(u_{\mathrm{E1P1}} - u_{\mathrm{B1P1}}) - k_2(u_{\mathrm{B1P1}} - u_{\mathrm{A1P1}}) \end{aligned} \tag{25}$$

in which, k_1 and k_2 are

$$k_1 = \frac{\sin(18^{\mathrm{o}})}{\sin(144^{\mathrm{o}})} k_2 = \frac{\sin(54^{\mathrm{o}})}{\sin(72^{\mathrm{o}})}. \tag{26}$$

Substitute (23) and (24) into (25), the voltage u_{A1P1} can be obtained

$$u_{\mathrm{A1P1}} = \left(\frac{2-2k_1}{k_2} - 1\right) U_{\mathrm{d}} + \left(\frac{1-k_1}{2k_2}\right) u_{\mathrm{o}}. \tag{27}$$

Similarly, the voltage u_{C1P1} and u_{D1P1} can be expressed as

$$\begin{cases} u_{\mathrm{C1P1}} = (\frac{2-3k_1}{-k_1})U_{\mathrm{d}} + (\frac{1-2k_1}{-2k_1})u_{\mathrm{o}} \\ u_{\mathrm{D1P1}} = (\frac{2k_1}{k_2} - \frac{2-3k_1}{k_1})U_{\mathrm{d}} + (\frac{k_1}{2k_2} - \frac{1-2k_1}{2k_1})u_{\mathrm{o}}. \end{cases} \tag{28}$$

Substitute (23), (27), and (28) into (22), the voltage $u_{\mathrm{An},20}$ in the interval [φ, $\varphi + 18^{\mathrm{o}}$) can be calculated as

$$u_{\mathrm{An},20} = \left(\frac{4-5k_1}{10k_2} + \frac{1}{5k_1} - \frac{1}{2}\right)(u_{\mathrm{o}} + 4U_{\mathrm{d}}). \tag{29}$$

Similarly, the level values in the other 19 combinations can also be determined, Fig. 10 is the waveform of $u_{\mathrm{An},20}$, and its level values of each step are shown in Table II. In Table II, the interval range represented by each mode is consistent with that in Table I.

TABLE III
MAIN PARAMETERS OF THE SIMULATION AND EXPERIMENT

Parameter	Value
RMS value of the voltage source	220V (50Hz)
Proportional *Coefficient K*	3:1
Load resistance	80Ω
Filtering inductor L_{s}	10mH
Capacitors C_{p} and C_{q}	3300μF/450V

From Table II, the Fourier series of voltage $u_{\mathrm{An},20}$ is

$$u_{\mathrm{An},20} = U_{\mathrm{s1},20}\left\{\sin(\omega t - \varphi) + \sum_{k=1}^{\infty} \frac{1}{20k \pm 1} \sin[(20k \pm 1)(\omega t - \varphi)]\right\} \tag{30}$$

where the fundamental voltage amplitude $U_{\mathrm{s1},20}$ of the voltage $u_{\mathrm{An},20}$ is

$$\begin{aligned} U_{\mathrm{s1},20} = \frac{4}{\pi}[&L_1(-\cos 18^{\mathrm{o}} + \cos 0^{\mathrm{o}}) + L_2(-\cos 36^{\mathrm{o}} + \cos 18^{\mathrm{o}}) \\ &+ L_3(-\cos 54^{\mathrm{o}} + \cos 36^{\mathrm{o}}) + L_4(-\cos 72^{\mathrm{o}} + \cos 54^{\mathrm{o}}) \\ &+ L_5(-\cos 90^{\mathrm{o}} + \cos 72^{\mathrm{o}})] \approx 0.2649(u_{\mathrm{o}} + 4U_{\mathrm{d}}). \end{aligned} \tag{31}$$

According to (30), the harmonic order contained in voltage $u_{\mathrm{An},20}$ is $(20k \pm 1)$th, k is a positive integer. The lowest harmonic is 19th, and its amplitude is about 5.26% of the amplitude of the fundamental wave.

From the above-mentioned analysis, if the equivalent current source model shown in Fig. 8 is established, the voltage $u_{\mathrm{An},20}$ is in phase with the current i_{a}, and the waveform is consistent with that in Fig. 10. When the primary and secondary voltages of the transformer meet the theoretical settings, the level values of each step are consistent with Table II.

C. Simulation and Experimental Verifications of the Equivalent Model

In order to verify the correctness of the equivalent model, this section carries out corresponding simulation and experimental verifications for a 1.85-kW prototype. Table III gives the main parameters of simulation and experiment.

Fig. 11 shows the input voltage and frequency spectrum of the phase-shifting transformer. In the simulation results shown in Fig. 11(a) and (b), the input voltage is a 12-step wave with the THD value of 8%, and the main harmonic order is $(20k \pm 1)$th (k is a positive integer), which conforms to theoretical analysis. In experimental results shown in Fig. 11(c) and (d), the input voltage THD value is slightly smaller than the simulated value, which is about 3.32%. From the harmonic ratio list, it can be seen that the main harmonics are the low-order harmonics and $(20k \pm 1)$th harmonics.

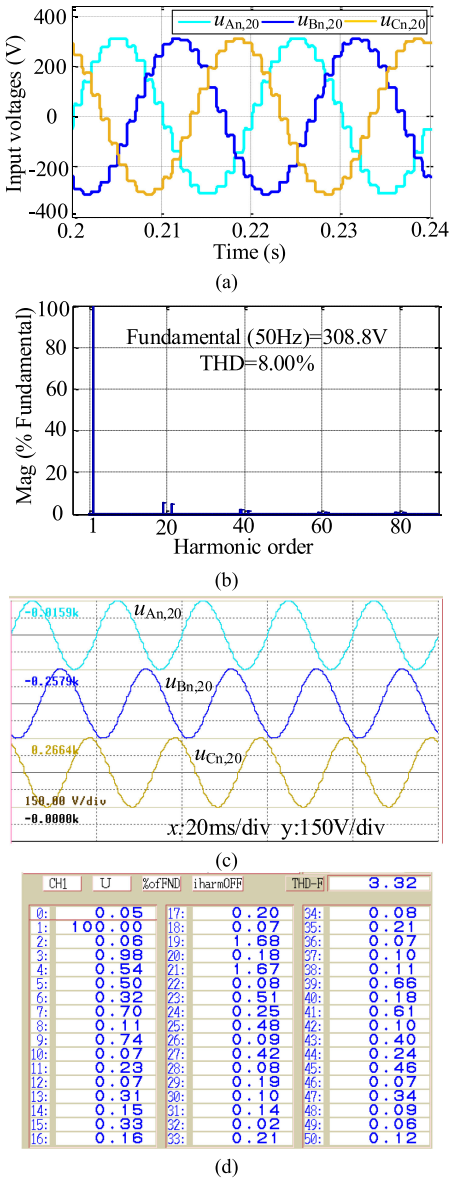

Fig. 11. Input voltages of the phase-shifting transformer. (a) Simulation waveforms. (b) Simulation spectrum. (c) Experimental waveforms. (d) Experimental spectrum.

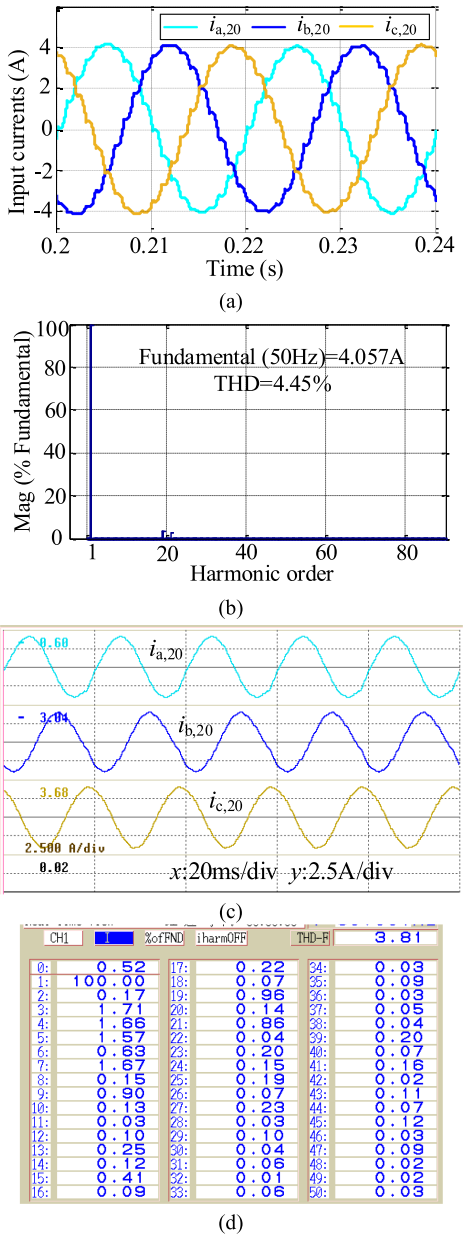

Fig. 12. Input currents of the phase-shifting transformer. (a) Simulation waveforms. (b) Simulation spectrum. (c) Experimental waveforms. (d) Experimental spectrum.

Fig. 12 shows the input current and frequency spectrum of the rectifier, which are approximate sine waves composed of 12 arcs in each phase. In simulation, the THD value of input current i_a is 4.45%, and the experimental value is slightly smaller than the simulated value, which is about 3.81%.

Comparing waveforms shown in Figs. 11 and 12, it is obvious that the input voltage and current of the phase-shifting transformer are in the same phase. Comparing the voltage and current spectrums, the order of higher content harmonics in the voltage are basically same with that in the current, and the voltage harmonics also influence the content of the current harmonic with the corresponding order, which indicates that reducing the harmonics in the input voltage can help to improve the quality of the input current.

The input currents i_{a1} and i_{a2} of the five-phase bridge rectifiers are shown in Fig. 13. The phase difference between the input currents of phase "a1" and phase "a2" is about 18°, so that the phase shift angle is in line with the transformer design. In one power cycle, each diode in the five-phase bridge rectifiers conducts 72°, which is consistent with the operating modes derived from the equivalent model.

The output current (i_{Rec1} and i_{Rec2}) waveforms of the five-phase bridge rectifiers are shown in Fig. 14, which are 10-pulse waveforms with the same rms value and a phase difference of 18°. The phase relationship is consistent with the assumption in the equivalent current source model shown in Fig. 9. Therefore, the equivalent current source model is suitable for this type of

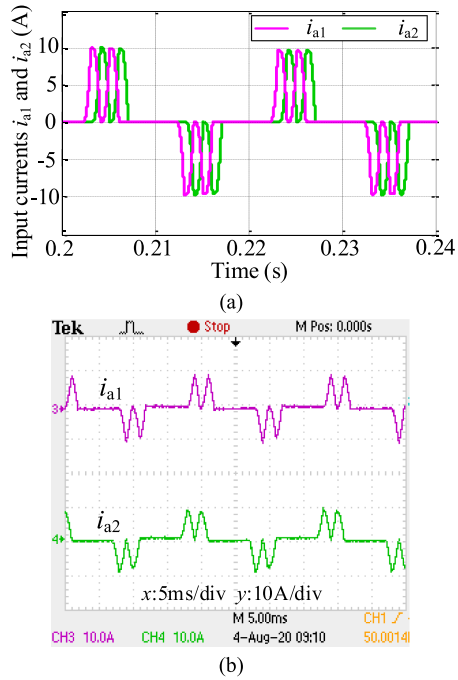

Fig. 13. Input currents i_{a1} and i_{a2} of the five-phase bridge rectifiers. (a) Simulation waveforms. (b) Experimental waveforms.

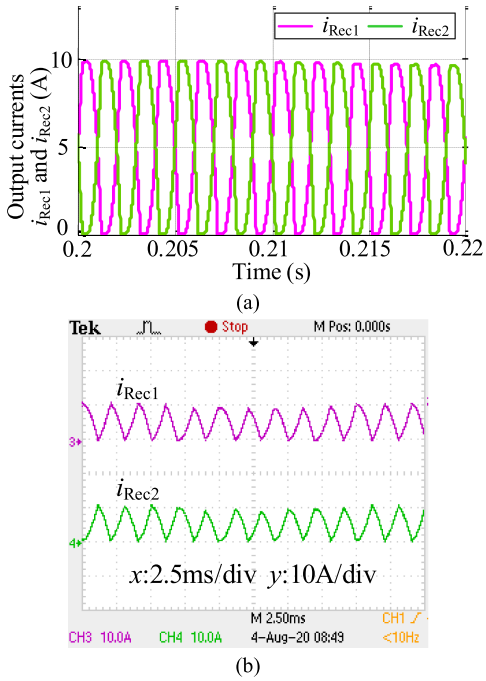

Fig. 14. Output currents i_{Rec1} and i_{Rec2} of the five-phase bridge rectifiers. (a) Simulation waveforms. (b) Experimental waveforms.

rectifier, and the operation mode of the HRC in the subsequent research can be analyzed based on this.

Fig. 15 shows the load voltage and current of the rectifier. Due to the existence of the dc side capacitors, the load voltage can be seen as constant with the rms value of about 385 V; under the condition of resistance load, the load current is also

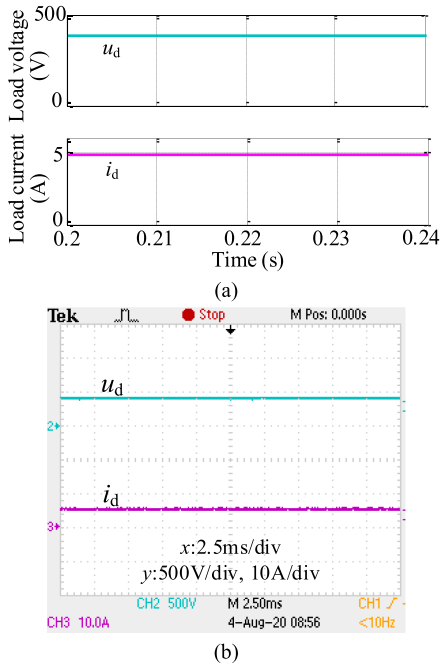

Fig. 15. Load voltage and current of the 20-pulse rectifier. (a) Simulation waveforms. (b) Experimental waveforms.

approximately constant with the rms value about 4.8 A so that the output power of the rectifier is about 1.85 kW.

V. 40-Pulse Rectifier With DC Side Passive HRC

Based on the series-connected 20-pulse rectifier shown in Fig. 7, this section proposes a series-connected 40-pulse rectifier using a dc side passive HRC, as shown in Fig. 16.

In Fig. 16, the passive HRC consists of a single-phase harmonic injection transformer and a single-phase full-wave rectifier. The primary side of the single-phase harmonic injection transformer T_{MP1} is connected between the midpoints M of the two groups of five-phase rectifier bridges, and the midpoint P_1 of the dc side capacitors C_p and C_q, the secondary side is connected to the ac side of the single-phase full-wave rectifier. The turns ratio of the transformer is N_p:N_s. The dc side of the single-phase full-wave rectifier is connected in parallel to both ends of the load. Fig. 17 shows the winding configuration of the harmonic injection transformer T_{MP1}.

A. Operation Modes Analysis of the 40-Pulse Rectifier

From the theoretical analysis and experimental results in Section III, the equivalent current source waveform shown in Fig. 9 can accurately describe the output current characteristics of the two five-phase bridge rectifiers. After using the HRC, the waveforms of the currents i_{Rec1} and i_{Rec2} are still approximately ten-pulse waves with a phase difference of 18°, which is consistent with the waveform shown in Fig. 9. Therefore, the equivalent model of the rectifier can be established according to Figs. 9 and 16, and the operating mode of the dc side passive HRC can be analyzed according to the relative magnitude relationship of the current i_{Rec1} and i_{Rec2} in each interval.

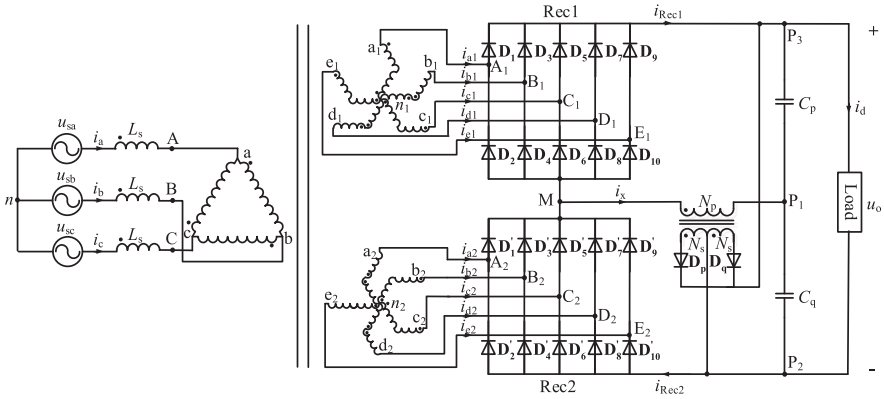

Fig. 16. 40-pulse rectifier with dc side passive HRC.

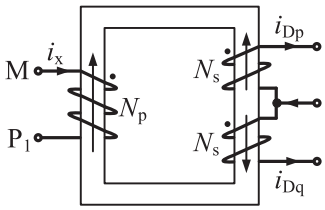

Fig. 17. Winding configuration of the harmonic injection transformer.

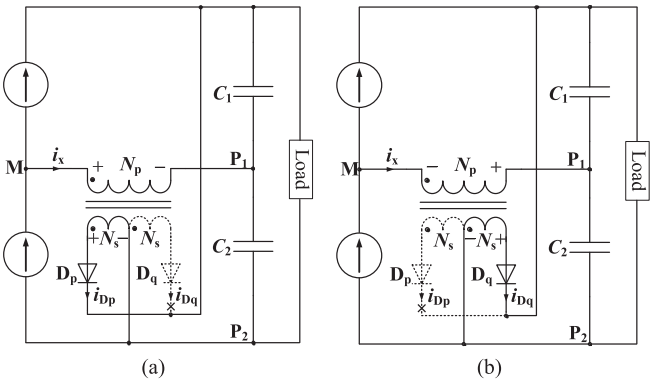

Fig. 18. Operation modes of the HRC. (a) Operation Mode I. (b) Operation Mode II.

Fig. 18 shows the two operation modes of the single-phase full-wave rectifier in the harmonic injection circuit.

According to the current reference direction shown in Fig. 18 and the identification of the dotted terminal of the harmonic injection transformer. When $i_{\mathrm{Rec1}} < i_{\mathrm{Rec2}}$, the current difference $i_{\mathrm{x}} > 0$, and flows into the dotted terminal of the primary winding of the passive harmonic injection transformer, while its secondary current flows out of the dotted terminal.

In the single-phase full-wave rectifier, the diode D_{p} is turned ON, and D_{q} is turned OFF so that the primary winding voltage u_{MP1} of the passive harmonic injection transformer $\mathrm{T_{MP1}}$ can be expressed as

$$u_{\mathrm{MP1}} = \frac{N_{\mathrm{p}}}{N_{\mathrm{s}}}\left(u_{\mathrm{o}} + U_{\mathrm{d}}\right). \tag{32}$$

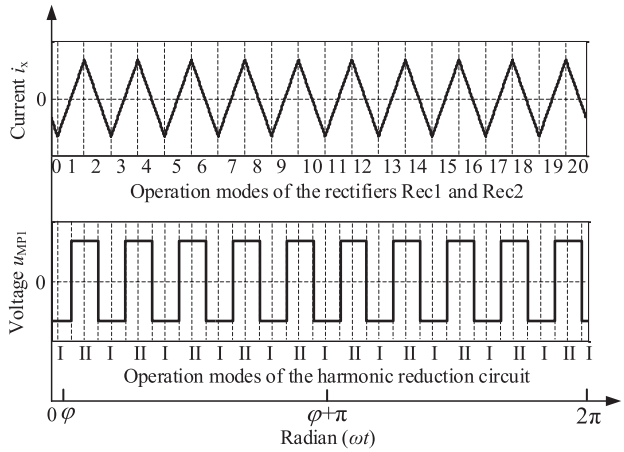

Fig. 19. Formation process of the square wave injection voltage u_{MP1}.

When $i_{\mathrm{Rec1}} > i_{\mathrm{Rec2}}$, the current difference $i_{\mathrm{x}} < 0$, and flows out of the dotted terminal of the primary winding, while its secondary current flows into the dotted terminal.

In the single-phase full-wave rectifier, the diode D_{p} is turned OFF, and D_{q} is turned ON so that the primary winding voltage u_{MP1} of the passive harmonic injection transformer $\mathrm{T_{MP1}}$ can be expressed as

$$u_{\mathrm{MP1}} = -\frac{N_{\mathrm{p}}}{N_{\mathrm{s}}}\left(u_{\mathrm{o}} + U_{\mathrm{d}}\right). \tag{33}$$

To facilitate analysis, define that

$$u_{\mathrm{x}} = -\frac{N_{\mathrm{p}}}{N_{\mathrm{s}}}\left(u_{\mathrm{o}} + U_{\mathrm{d}}\right). \tag{34}$$

Based on the above-mentioned analysis, the primary side of the injection transformer can generate a ten times power frequency square wave voltage with the level value of $\pm u_{\mathrm{x}}$. The formation process of the square wave and the corresponding phase relations are shown in Fig. 19. Each operation mode of the five-phase bridge rectifiers corresponds to two operation modes of the HRC.

From Fig. 19, the operating mode of the 40-pulse rectifier is the operating mode of the 20-pulse rectifier superimposed on the operating modes of the HRC.

B. Harmonic Reduction Mechanism Analysis

For the sake of simplicity, select interval [φ+36°, φ+54°) as an example to analyze the rectifier voltage.

Based on Figs. 16 and 19, in combination with KVL, the rectifier voltages fulfill

$$\begin{cases} u_{\mathrm{E1P1}} = U_{\mathrm{d}} + \frac{u_{\mathrm{o}}}{2} \\ u_{\mathrm{C1P1}} = -U_{\mathrm{d}} + u_{\mathrm{MP1}} \end{cases} \quad \begin{cases} u_{\mathrm{A2P2}} = U_{\mathrm{d}} + u_{\mathrm{MP1}} + \frac{u_{\mathrm{o}}}{2} \\ u_{\mathrm{C2P2}} = -U_{\mathrm{d}}. \end{cases} \tag{35}$$

From (35) and the principle of phasor synthesis, the voltage u_{A2C2} is

$$\begin{aligned} u_{\mathrm{A2C2}} &= u_{\mathrm{A2P2}} - u_{\mathrm{C2P2}} = u_{\mathrm{A2n2}} - u_{\mathrm{C2n2}} \\ &= 2U_{\mathrm{d}} + u_{\mathrm{MP1}} + \frac{u_{\mathrm{o}}}{2}. \end{aligned} \tag{36}$$

Combined with the phasor diagram of the phase-shifting transformer shown in Fig. 4, the phase voltages u_{A2n2} and u_{C2n2} can be expressed as

$$\begin{aligned} u_{\mathrm{A2n2}} &= \begin{cases} k_1 u_{\mathrm{A1C1}} = k_1(u_{\mathrm{A1P1}} - u_{\mathrm{C1P1}}) \\ k_2 u_{\mathrm{E1D1}} = k_2(u_{\mathrm{E1P1}} - u_{\mathrm{D1P1}}) \end{cases} \\ u_{\mathrm{C2n2}} &= \begin{cases} k_1 u_{\mathrm{C1E1}} = k_1(u_{\mathrm{C1P1}} - u_{\mathrm{E1P1}}) \\ k_2 u_{\mathrm{B1A1}} = k_2(u_{\mathrm{B1P1}} - u_{\mathrm{A1P1}}) \end{cases} \end{aligned} \tag{37}$$

where k_1 and k_2 still satisfy (11).

Substitute (35) and (37) into (36), the voltages u_{A1P1}, u_{B1P1}, and u_{D1P1} are

$$\begin{cases} u_{\mathrm{A1P1}} = (\frac{2}{k_1} - 3)U_{\mathrm{d}} + (\frac{1}{k_1} + 2)u_{\mathrm{MP1}} + (\frac{1}{2k_1} - \frac{1}{2})u_{\mathrm{o}} \\ u_{\mathrm{B1P1}} = (\frac{2}{k_1} - \frac{2k_1}{k_2} - 3)U_{\mathrm{d}} + (\frac{1}{k_1} + \frac{k_1}{k_2} + 2)u_{\mathrm{MP1}} \\ \qquad + (\frac{1}{2k_1} - \frac{k_1}{2k_2} - \frac{1}{2})u_{\mathrm{o}} \\ u_{\mathrm{D1P1}} = (\frac{2k_1+k_2-2}{k_2})U_{\mathrm{d}} + (\frac{-k_1-1}{k_2})u_{\mathrm{MP1}} + (\frac{k_1+k_2-1}{2k_2})u_{\mathrm{o}}. \end{cases} \tag{38}$$

Substitute (37) and (38) into (22), the input voltage $u_{\mathrm{An,40}}$ in this interval is

$$\begin{aligned} u_{\mathrm{An,40}} = &\left(\frac{3}{5k_1} + \frac{1}{5k_2} + 1\right) u_{\mathrm{MP1}} + \left(\frac{3}{10k_1} + \frac{1}{10k_2} - \frac{1}{2}\right) \\ &\times (u_{\mathrm{o}} + 4U_{\mathrm{d}}). \end{aligned} \tag{39}$$

In combination with Fig. 19, the piecewise function of the voltage $u_{\mathrm{An,40}}$ can be obtained as shown in Appendix (63).

Similarly, the level values of voltage $u_{\mathrm{An,40}}$ in the other 38 cases can be obtained.

Fig. 20 shows the waveform of voltage $u_{\mathrm{An,40}}$. Some of the step level values are shown in Table IV. Since this waveform has a quarter symmetry characteristic, other step level values can be obtained by symmetry.

Comparing Table II with Table IV, it can be observed that, after using passive HRC, the original intervals are equally divided into two subintervals based on the operating modes of the passive HRC. A square wave voltage with an amplitude of $\pm u_{\mathrm{MP1}}$ is injected into the dc side of the five-phase rectifier bridge. Then, a voltage related to u_{MP1} can be generated and added to the input voltage of the transformer, thereby increasing the number of steps and reducing the harmonic content.

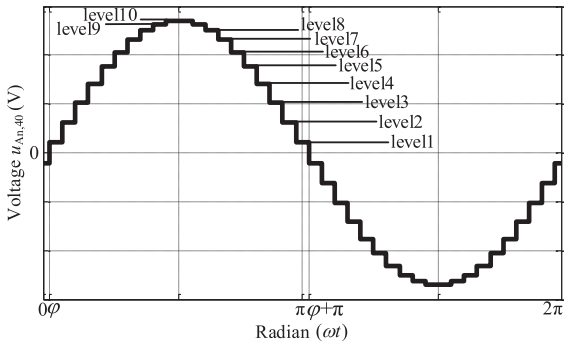

Fig. 20. Waveform of the input voltage $u_{\mathrm{An,40}}$.

TABLE IV
LEVEL VALUES OF THE INPUT VOLTAGE $U_{\mathrm{An,20}}$

Voltage	Level Value
level1	$(\frac{2-5k_1}{10k_1}+\frac{4-5k_1}{10k_2})(u_{\mathrm{o}}+4U_{\mathrm{d}})-\frac{N_{\mathrm{p}}}{N_{\mathrm{s}}}(\frac{2+5k_1}{5k_1}+\frac{4+5k_1}{5k_2})(u_{\mathrm{o}}+U_{\mathrm{d}})$
level2	$(\frac{2-5k_1}{10k_1}+\frac{4-5k_1}{10k_2})(u_{\mathrm{o}}+4U_{\mathrm{d}})+\frac{N_{\mathrm{p}}}{N_{\mathrm{s}}}(\frac{2+5k_1}{5k_1}+\frac{4+5k_1}{5k_2})(u_{\mathrm{o}}+U_{\mathrm{d}})$
level3	$(\frac{-3+5k_1}{10k_1}+\frac{-1+5k_1}{10k_2})(u_{\mathrm{o}}+4U_{\mathrm{d}})-\frac{N_{\mathrm{p}}}{N_{\mathrm{s}}}(\frac{3+5k_1}{5k_1}+\frac{1+5k_1}{5k_2})(u_{\mathrm{o}}+U_{\mathrm{d}})$
level4	$(\frac{-3+5k_1}{10k_1}+\frac{-1+5k_1}{10k_2})(u_{\mathrm{o}}+4U_{\mathrm{d}})+\frac{N_{\mathrm{p}}}{N_{\mathrm{s}}}(\frac{3+5k_1}{5k_1}+\frac{1+5k_1}{5k_2})(u_{\mathrm{o}}+U_{\mathrm{d}})$
level5	$(\frac{3-5k_1}{10k_1}+\frac{1}{10k_2})(u_{\mathrm{o}}+4U_{\mathrm{d}})-\frac{N_{\mathrm{p}}}{N_{\mathrm{s}}}(\frac{3+5k_1}{5k_1}+\frac{1}{5k_2})(u_{\mathrm{o}}+U_{\mathrm{d}})$
level6	$(\frac{3-5k_1}{10k_1}+\frac{1}{10k_2})(u_{\mathrm{o}}+4U_{\mathrm{d}})+\frac{N_{\mathrm{p}}}{N_{\mathrm{s}}}(\frac{3+5k_1}{5k_1}+\frac{1}{5k_2})(u_{\mathrm{o}}+U_{\mathrm{d}})$
level7	$(\frac{-2+5k_1}{10k_1}+\frac{1}{10k_2})(u_{\mathrm{o}}+4U_{\mathrm{d}})-\frac{N_{\mathrm{p}}}{N_{\mathrm{s}}}(\frac{2+5k_1}{5k_1}-\frac{1}{5k_2})(u_{\mathrm{o}}+U_{\mathrm{d}})$
level8	$(\frac{-2+5k_1}{10k_1}+\frac{1}{10k_2})(u_{\mathrm{o}}+4U_{\mathrm{d}})+\frac{N_{\mathrm{p}}}{N_{\mathrm{s}}}(\frac{2+5k_1}{5k_1}-\frac{1}{5k_2})(u_{\mathrm{o}}+U_{\mathrm{d}})$
level9	$(\frac{1}{5k_1}-\frac{1}{10k_2})(u_{\mathrm{o}}+4U_{\mathrm{d}})-\frac{N_{\mathrm{p}}}{N_{\mathrm{s}}}(\frac{2}{5k_1}-\frac{1}{5k_2})(u_{\mathrm{o}}+U_{\mathrm{d}})$
level10	$(\frac{1}{5k_1}-\frac{1}{10k_2})(u_{\mathrm{o}}+4U_{\mathrm{d}})+\frac{N_{\mathrm{p}}}{N_{\mathrm{s}}}(\frac{2}{5k_1}-\frac{1}{5k_2})(u_{\mathrm{o}}+U_{\mathrm{d}})$

C. Optimized Design of the Harmonic Injection Transformer

Assuming that the turns ratio of the primary and secondary windings of the harmonic injection transformer $\mathrm{T_{MP1}}$ is N_{p}: N_{s} = 1: n, from Table IV, the effective value $U_{\mathrm{An,40}}$ of the voltage $u_{\mathrm{An,40}}$ and the fundamental voltage amplitude $U_{\mathrm{s1,40}}$ can be obtained

$$\begin{cases} U_{\mathrm{An,40}} = \sqrt{\frac{1}{5}[A(u_{\mathrm{o}}+4U_{\mathrm{d}})^2 + B(\frac{u_{\mathrm{o}}+U_{\mathrm{d}}}{n})^2]} \\ U_{\mathrm{s1,40}} = \frac{4}{\pi}[(C+D)(u_{\mathrm{o}}+4U_{\mathrm{d}}) + (E+F)(\frac{u_{\mathrm{o}}+U_{\mathrm{d}}}{n})] \end{cases} \tag{40}$$

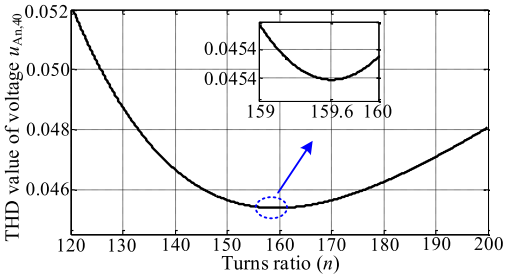

Fig. 21. Relationship curve between the THD and turns ratio n.

where A, B, C, D, E, and F are presented as (64) in Appendix.

Based on the definition of THD, the THD expression of the voltage $u_{\mathrm{An},40}$ is

$$\mathrm{THD}_{40} = \frac{\sqrt{2U_{\mathrm{An},40}^2 - U_{\mathrm{s1},40}^2}}{U_{\mathrm{s1},40}}. \tag{41}$$

Substitute (40) and (64) into (41), the relationship curve between the THD value of the voltage $u_{\mathrm{An},40}$ and the turns ratio n of the harmonic injection transformer can be plotted as shown in Fig. 21. From Fig. 21, when n is 159.6, THD takes the minimum value. The optimum turns ratio is consistent with that derived from (16).

D. Characteristic Analysis of the Input Current

In order to simplify the data processing process, the amplitude U_{s} of the three-phase ac voltage source is selected as the voltage reference value, and the ratio of the actual voltage value to the voltage reference value is the normalized voltage value. At the same time, define $U_{\mathrm{s}}/\omega L_{\mathrm{s}}$ as the current reference value, and the ratio of the actual current value to the current reference value is the normalized current value. After normalization, the voltage and current values are transformed into dimensionless expressions.

The normalized expressions of voltage source u_{sa}, inductor terminal voltage u_{Ls}, load voltage u_{o}, and diode conduction voltage drop U_{d} are

$$\begin{cases} u_{\mathrm{msa}} = \frac{u_{\mathrm{sa}}}{U_{\mathrm{s}}} \\ u_{\mathrm{mLs}} = \frac{u_{\mathrm{Ls}}}{U_{\mathrm{s}}} \end{cases} \quad \begin{cases} u_{\mathrm{mo}} = \frac{u_{\mathrm{o}}}{U_{\mathrm{s}}} \\ U_{\mathrm{md}} = \frac{U_{\mathrm{d}}}{U_{\mathrm{s}}}. \end{cases} \tag{42}$$

Taking phase "a" as an example, the normalized expressions of the grid-side input current i_{a}, the input current i_{a1} of the bridge rectifier Rec1, and the two sets output currents i_{Rec1} and i_{Rec2} of bridge rectifiers are

$$\begin{cases} i_{\mathrm{ja}} = \frac{\omega L_{\mathrm{s}}}{U_{\mathrm{s}}} i_{\mathrm{a}} \\ i_{\mathrm{ja1}} = \frac{\omega L_{\mathrm{s}}}{U_{\mathrm{s}}} i_{\mathrm{a1}} \end{cases} \quad \begin{cases} i_{\mathrm{jRec1}} = \frac{\omega L_{\mathrm{s}}}{U_{\mathrm{s}}} i_{\mathrm{Rec1}} \\ i_{\mathrm{jRec2}} = \frac{\omega L_{\mathrm{s}}}{U_{\mathrm{s}}} i_{\mathrm{Rec2}}. \end{cases} \tag{43}$$

From Fig. 16 and KVL, the terminal voltage of inductors L_{s} can be obtained

$$u_{\mathrm{Ls}} = L_{\mathrm{s}} \frac{\mathrm{d}i_{\mathrm{a}}}{\mathrm{d}t} = u_{\mathrm{sa}} - u_{\mathrm{An}}. \tag{44}$$

Substitute (42) and (43) into (44), the normalized expressions of voltage u_{mLs} is

$$u_{\mathrm{mLs}} = \frac{\mathrm{d}i_{\mathrm{ja}}}{\mathrm{d}(\omega t)} = \sin(\omega t) - u_{\mathrm{mAn}}. \tag{45}$$

Based on the half power cycle symmetry of i_{a}, doing integral operation on (45), the current i_{ja} fulfills

$$\int_{\varphi}^{\varphi+\pi} i_{\mathrm{ja}} \mathrm{d}(\omega t) = \int_{\varphi}^{\varphi+\pi} [\sin(\omega t) - u_{\mathrm{mAn}}] \mathrm{d}(\omega t) = 0. \tag{46}$$

In the phase-shifting transformer, assuming that the rms value of the input phase voltage U_{An} is equal to the rms value of the output phase voltage U_{A1n1}, combining the level values of u_{An} and (42), in the interval $[\varphi, \varphi+\pi]$, the normalized expression of voltage u_{An} is shown in Appendix (65).

In (65), α_1 and α_2 are

$$\begin{cases} \alpha_1 = (u_{\mathrm{mo}} + 4U_{\mathrm{md}}) \\ \alpha_2 = \frac{(u_{\mathrm{mo}} + U_{\mathrm{md}})}{n}. \end{cases} \tag{47}$$

From (46) and (65), the phase difference φ fulfills

$$\cos\varphi = \frac{\pi}{20}\left(\frac{2}{5k_1} + \frac{4}{5k_2}\right)\alpha_1 \tag{48}$$

that is

$$\varphi = \arccos\left[\frac{\pi}{20}\left(\frac{2}{5k_1} + \frac{4}{5k_2}\right)\alpha_1\right]. \tag{49}$$

If the corresponding voltage value in the interval $[\varphi + \frac{(i-1)\pi}{20}, \varphi + \frac{i\pi}{20}]$, i is an integer between 1 and 20, is marked as u_{mAni}, in combination with (45) and the initial value $i_{\mathrm{ja}}(\varphi) = 0$, the expression of i_{ja} in the interval $[\varphi, \varphi+\pi]$ can be determined as shown in Appendix (66).

In (66), S_1, S_2, S_3, …,S_{i} are

$$\begin{cases} S_1 = 0 \\ S_2 = S_1 + \frac{\pi}{20}(u_{\mathrm{mAn2}} - u_{\mathrm{mAn1}}) \\ S_3 = S_2 + \frac{\pi}{10}(u_{\mathrm{mAn3}} - u_{\mathrm{mAn2}}) \\ \vdots \\ S_{\mathrm{i}} = S_{(\mathrm{i}-1)} + \frac{(i-1)\pi}{20}\left[u_{\mathrm{mAni}} - u_{\mathrm{mAn(i-1)}}\right]. \end{cases} \tag{50}$$

From (47)–(50) and (65), the waveform of the input current i_{ja} can be plotted as shown in Fig. 22.

E. Simulation and Experimental Verifications of the Proposed Passive HRC

This section gives corresponding simulation and experimental verifications to verify the effectiveness of the proposed HRC.

The simulation and experimental parameter settings are consistent with Table III. In addition, the turns ratio n of the harmonic injection transformer T_{MP1} is 1:160.

Fig. 23 shows the input voltage and frequency spectrum of the phase-shifting transformer. From Fig. 23, it can be seen that the rectifier works in a 40-pulse rectification state. In the simulation, the input voltage THD value is 3.7%, the main harmonic order is $(40k \pm 1)$th, and k is a positive integer. In

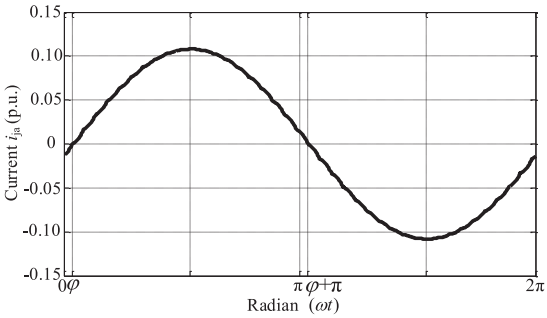

Fig. 22. Waveform of the input current i_{ja}.

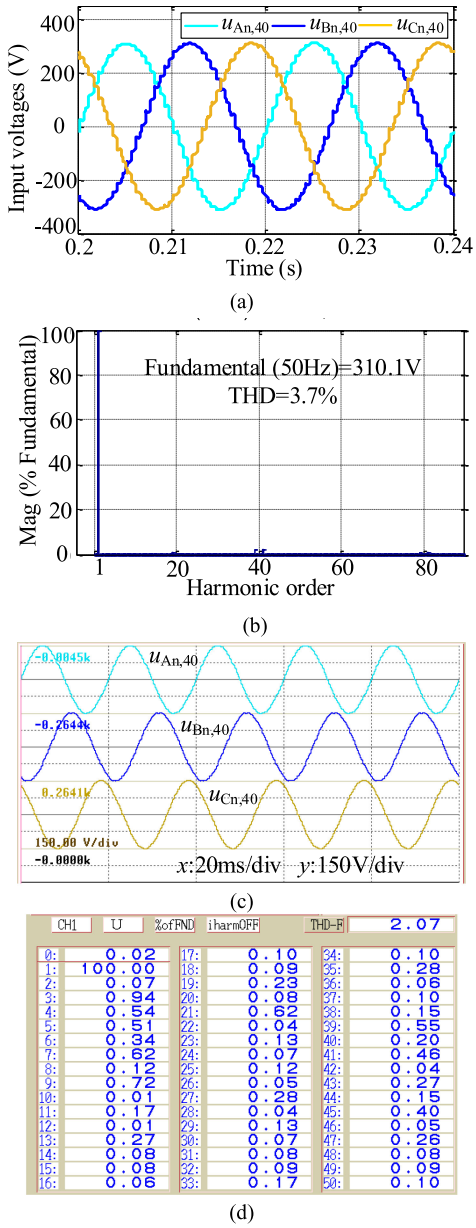

(a) (b) (c) (d)

Fig. 23. Input voltages of the phase-shifting transformer. (a) Simulation waveforms. (b) Simulation spectrum. (c) Experimental waveforms. (d) Experimental spectrum.

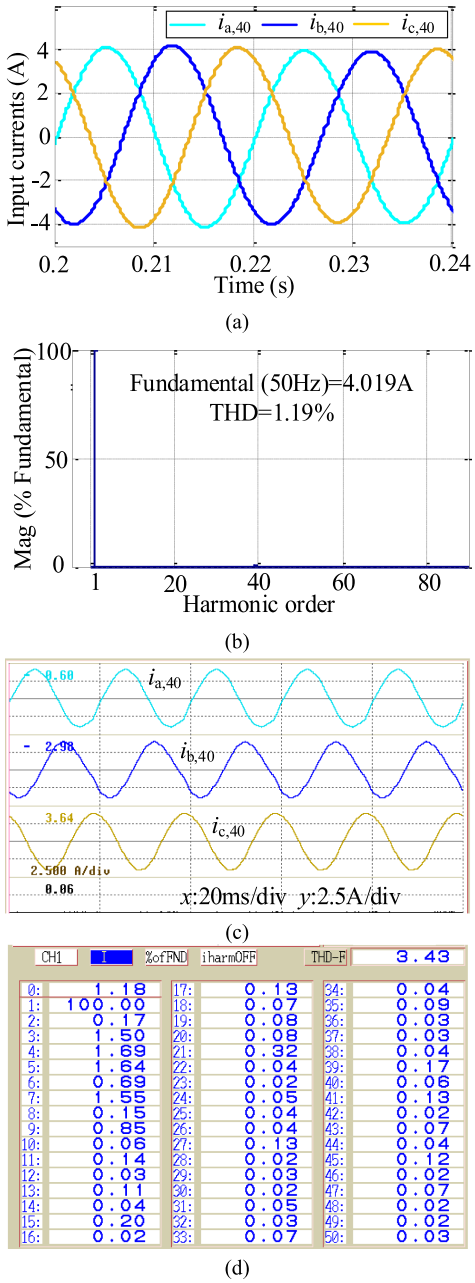

(a) (b) (c) (d)

Fig. 24. Input currents of the phase-shifting transformer. (a) Simulation waveforms. (b) Simulation spectrum. (c) Experimental waveforms. (d) Experimental spectrum.

the experiment, the input voltage THD value reduces to 2.07%. Comparing the frequency spectrum shown in Fig. 11(d), it can be seen that after using the harmonic suppression circuit, the 19th and 21st harmonic content is significantly reduced, and the other harmonics are suppressed in different degrees.

Fig. 24 shows the input current and frequency spectrum of the 40-pulse rectifier. In a power cycle, the input current is composed of 40 segments of arcs. Due to the existence of the ac side inductors, its THD value drops to a lower level. In the simulation, the THD value is 1.19%. In the experiment, the current waveform is near to the sine wave, and the THD value drops to 3.43%. The variation trend of input current harmonics is similar to that

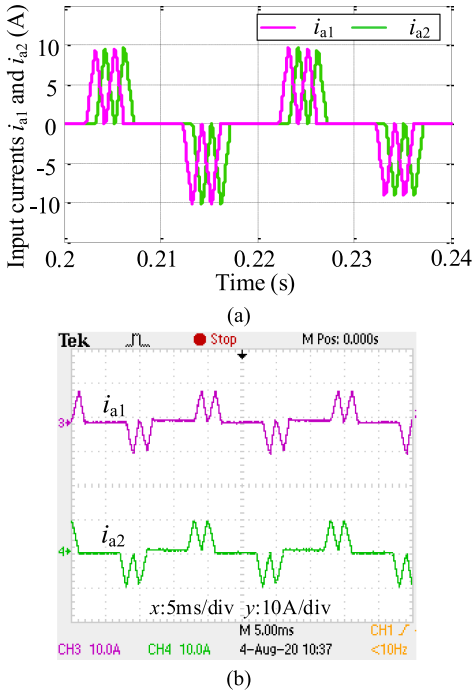

Fig. 25. Input currents i_{a1} and i_{a2} of the five-phase bridge rectifiers. (a) Simulation waveforms. (b) Experimental waveforms.

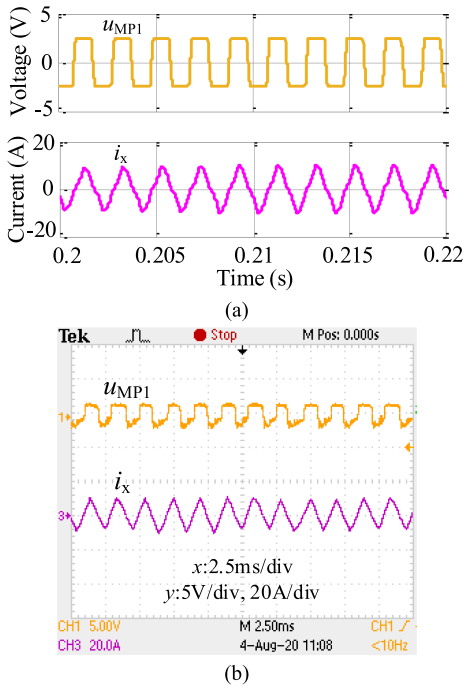

Fig. 26. Input currents i_{a1} and i_{a2} of the five-phase bridge rectifiers. (a) Simulation waveforms. (b) Experimental waveforms.

of voltage harmonics. After using the HRC, the 19th and 21st current harmonics are also obviously reduced.

Fig. 25 shows the input current waveforms of the bridge rectifiers, which are the same as that in the 20-pulse rectifier. In one power cycle, each diode in the five-phase bridge rectifiers conducts 72°, and the phase difference between phase "a1" and phase "a2" is 18°. This indicates that the use of the HRC does not change the operating modes of the five-phase bridge rectifiers, which conforms to the theoretical analysis results.

Fig. 26 shows the primary voltage and current waveforms of the harmonic injection transformer. It can be seen from Fig. 26 that both the voltage and current frequencies are 500 Hz, and the phase correspondence is consistent with the theoretical analysis results shown in Fig. 19. Therefore, the operating mode of the HRC can be accurately analyzed by using the equivalent current source model.

Fig. 27 shows the load voltage and current of the 40-pulse rectifier. At this time, the load voltage and current can still be regarded as constant with rms values of 384.5 V and 4.8 A, respectively, so that the rectifier load power is about 1.85 kW.

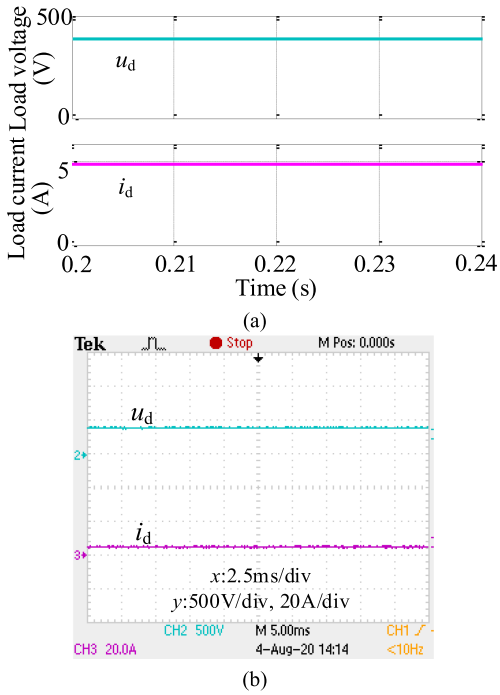

Fig. 27. Load voltage and current of the 40-pulse rectifier. (a) Simulation waveforms. (b) Experimental waveforms.

F. Calculations on kVA Rating of Magnetic Devices and Power Losses of Diodes

Based on the above-mentioned theoretical analysis and test results, the kVA rating of the proposed delta/double zigzag-connected phase-shifting transformer and the single-phase harmonic injection transformer are discussed. The conduction losses of the diodes in the main circuit and the auxiliary circuit are calculated.

The kVA rating of the phase-shifting transformer can be calculated by

$$S_{\mathrm{P-STr}} = \frac{1}{2}\sum\left(U_{\mathrm{winding}} I_{\mathrm{winding}}\right) \tag{51}$$

where U_{winding} is the rms value of the terminal voltage of each winding in the phase-shifting transformer and I_{winding} is the rms value of the current flowing through each winding in this transformer.

Based on the winding configuration of the transformer, the rms value of the terminal voltage of the primary winding is

$$U_{\text{primary}} = \sqrt{3}KU_{\text{A1n1}}. \tag{52}$$

K is equal to 3 in this design.

Substitute the optimum turns ratio $n = 160$ into (40), in combination with (26) and (64), it can be obtained that the relationship between U_{A1n1} and the load voltage U_{o} is

$$U_{\text{A1n1}} \approx 0.19U_{\text{o}}. \tag{53}$$

The rms values of the secondary winding terminal voltages can be determined by turns ratio relations as shown in (62).

In order to simplify calculations, assuming that output phase currents of phase-shifting transformer are triangle waves, and defining that the peak current of the phase current is i_{peak}. In combination with test results presented in Figs. 25 and 27, the peak current i_{peak} is about two times of load current I_{o}. Based on the above-mentioned conditions, the rms value of the current flowing through the secondary winding is

$$\begin{aligned} I_{\text{secondary}} &= \sqrt{\frac{1}{2\pi}\int_0^{2\pi} i_{\text{a1}}^2 \mathrm{d}(\omega t)} \\ &= \sqrt{\frac{8}{2\pi}\cdot i_{\text{peak}}^2 \cdot \left(\frac{10}{\pi}\right)^2 \int_0^{\frac{\pi}{10}} (\omega t)^2 \mathrm{d}(\omega t)} \\ &\approx 0.36 i_{\text{peak}} \approx 0.72 I_{\text{o}}. \end{aligned} \tag{54}$$

Based on the winding configuration shown in Fig. 6 and the ampere-turns balance law, the current flowing through the primary winding fulfills

$$I_{\text{primary}} \approx 0.34 I_{\text{o}}. \tag{55}$$

Based on the above-mentioned analysis, it can be obtained that

$$\begin{aligned} S_{\text{P-STr}} = \frac{1}{2}\Bigg[& 3U_{\text{primary}}I_{\text{primary}} + \frac{2U_{\text{primary}}}{\sqrt{3}K\sin 120^{\text{o}}} \\ & \times (\sin 30^{\text{o}} + \sin 54^{\text{o}} + \sin 18^{\text{o}} + \sin 48^{\text{o}} + \sin 36^{\text{o}} \\ & + \sin 12^{\text{o}} + \sin 42^{\text{o}} + \sin 6^{\text{o}} + \sin 24^{\text{o}}) I_{\text{secondary}} \\ & + \frac{U_{\text{primary}} I_{\text{secondary}}}{\sqrt{3}K} \Bigg] \\ \approx & \ 129.8\% U_{\text{o}} I_{\text{o}}. \end{aligned} \tag{56}$$

So that the kVA rating of the phase-shifting transformer takes about 129.8% of the load power.

The conduction losses for each diode in the five-phase diode bridge rectifiers in one cycle is

$$P_{\text{loss-diode}} = U_{\text{forward-drop}} I_{\text{D}} \tag{57}$$

where $U_{\text{forward-drop}}$ is the forward drop for diode and I_{D} is the current flowing through the diode with the rms value of $0.5I_{\text{secondary}}$.

When takes $U_{\text{forward-drop}}$ as 0.7 V, under test conditions in this article, the total power losses for each diode in the main circuit is about 1.2 VA per cycle.

The kVA rating of the phase-shifting transformer can be calculated by

$$S_{\text{H-ITr}} = \frac{1}{2}(U_{\text{MP1}} I_{\text{x}} + 2U_{\text{o}} I_{\text{Dp}}) \tag{58}$$

where U_{MP1}, I_{x}, and I_{Dp} are all rms values.

According to the optimum turns ratio design of this harmonic injection transformer and operation modes of the harmonic injection circuit, it can be determined that

$$\begin{cases} U_{\text{MP1}} = \frac{U_{\text{o}}}{160} \\ I_{\text{x}} \approx \frac{\sqrt{3}}{3} i_{\text{peakx}} \\ I_{\text{Dp}} \approx \frac{I_{\text{x}}}{160\sqrt{2}} \end{cases} \tag{59}$$

from test results shown in Figs. 26 and 27, the peak value of current i_{x} is about $2I_{\text{o}}$.

Substitute (59) into (58), it can be obtained that

$$S_{\text{H-ITr}} \approx 0.87\% U_{\text{o}} I_{\text{o}}. \tag{60}$$

The conduction losses for D_p or D_q in one cycle is

$$P_{\text{loss-Dp}} = U_{\text{forward-drop}} I_{\text{Dp}}. \tag{61}$$

When takes $U_{\text{forward-drop}}$ as 0.7 V, under test conditions in this article, the total power losses for each diode in the auxiliary circuit is about 0.017 VA per cycle. So that the kVA rating of the harmonic injection transformer and the power losses of the diodes in the auxiliary circuit are at a quite low level. The cost of HRC is quite low.

VI. Conclusion

This article combines two methods of increasing the phase number of bridge rectifier and using the dc side HRC to improve the power quality of the rectifier. The optimum turns ratio of harmonic injection transformer for the 8*N*-pulse rectifier is derived, and its effectiveness is verified in the proposed 40-pulse rectifier (*N* is equal to five). The optimum turns ratio determined from the general calculation formula is consistent with that obtained based on the conventional method. Compared with the two methods, the novel method can avoid complex calculations and has a certain universality.

Simulation and experimental results indicate that the delta-double zigzag phase-shifting transformer designed in this article is suitable for five-phase bridge rectifiers, and the equivalent current source model can accurately describe the operating mode of the rectifier. Based on this model, the theoretical calculation of the voltage step values is presented in detail; the passive harmonic reduction mechanism is summarized by comparing the main voltage variations in the 20-pulse rectifier and the 40-pulse rectifier. When the turns ratio of the harmonic injection transformer is reasonably designed, the rectifier has a good harmonic reduction effect. In addition, the proposed HRC only uses passive components with properties of simple structure, lower capacity, and easy implementation.

APPENDIX

$$\begin{bmatrix} N_{\mathrm{a1}} \\ N_{\mathrm{a2}} \\ N_{\mathrm{a3}} \\ N_{\mathrm{a4}} \\ N_{\mathrm{a5}} \\ N_{\mathrm{a6}} \end{bmatrix} = \frac{N_{\mathrm{a}}}{\sqrt{3}K\sin 120^{\mathrm{o}}} \begin{bmatrix} \sin 30^{\mathrm{o}} \\ \sin 54^{\mathrm{o}} \\ \sin 18^{\mathrm{o}} \\ \sin 48^{\mathrm{o}} \\ \sin 36^{\mathrm{o}} \\ \sin 12^{\mathrm{o}} \end{bmatrix} \begin{bmatrix} N_{\mathrm{b1}} \\ N_{\mathrm{b2}} \\ N_{\mathrm{b3}} \\ N_{\mathrm{b4}} \\ N_{\mathrm{b5}} \\ N_{\mathrm{b6}} \end{bmatrix} = \frac{N_{\mathrm{b}}}{\sqrt{3}K\sin 120^{\mathrm{o}}} \begin{bmatrix} \sin 42^{\mathrm{o}} \\ \sin 6^{\mathrm{o}} \\ \sin 6^{\mathrm{o}} \\ \sin 42^{\mathrm{o}} \\ \sin 24^{\mathrm{o}} \\ \sin 24^{\mathrm{o}} \end{bmatrix} \begin{bmatrix} N_{\mathrm{c1}} \\ N_{\mathrm{c2}} \\ N_{\mathrm{c3}} \\ N_{\mathrm{c4}} \\ N_{\mathrm{c5}} \\ N_{\mathrm{c6}} \end{bmatrix} = \frac{N_{\mathrm{a}}}{\sqrt{3}K\sin 120^{\mathrm{o}}} \begin{bmatrix} \sin 30^{\mathrm{o}} \\ \sin 18^{\mathrm{o}} \\ \sin 54^{\mathrm{o}} \\ \sin 12^{\mathrm{o}} \\ \sin 36^{\mathrm{o}} \\ \sin 48^{\mathrm{o}} \end{bmatrix} \tag{62}$$

$$N_{\mathrm{b7}} = \frac{N_{\mathrm{b}}}{\sqrt{3}K}$$

$$u_{\mathrm{An},40} = \begin{cases} -\frac{N_{\mathrm{p}}}{N_{\mathrm{s}}}(\frac{3}{5k_1} + \frac{1}{5k_2} + 1)(u_{\mathrm{o}} + U_{\mathrm{d}}) + (\frac{3}{10k_1} + \frac{1}{10k_2} - \frac{1}{2})(u_{\mathrm{o}} + 4U_{\mathrm{d}}) \omega t \in [\varphi + 36^{\mathrm{o}}, \varphi + 45^{\mathrm{o}}) \\ \frac{N_{\mathrm{p}}}{N_{\mathrm{s}}}(\frac{3}{5k_1} + \frac{1}{5k_2} + 1)(u_{\mathrm{o}} + U_{\mathrm{d}}) + (\frac{3}{10k_1} + \frac{1}{10k_2} - \frac{1}{2})(u_{\mathrm{o}} + 4U_{\mathrm{d}}) \omega t \in [\varphi + 45^{\mathrm{o}}, \varphi + 54^{\mathrm{o}}) \end{cases} \tag{63}$$

$$\begin{cases} A = \frac{10k_1^2 - 10k_1 + 3}{10k_1^2} + \frac{5k_1^2 - 5k_1 + 2}{10k_2^2} + \frac{5k_1^2 - 5k_1 + 1}{5k_1 k_2} \\ B = \frac{20k_1^2 + 20k_1 + 6}{5k_1^2} + \frac{10k_1^2 + 10k_1 + 4}{5k_2^2} + \frac{20k_1^2 + 20k_1 + 4}{5k_1 k_2} \\ C = \frac{1}{10k_1}[(10k_1 - 5)\cos\frac{\pi}{10} + (-10k_1 + 6)\cos\frac{\pi}{5} + (10k_1 - 5)\cos\frac{3\pi}{10} + (-5k_1 + 4)\cos\frac{2\pi}{5} - 5k_1 + 2] \\ D = \frac{1}{10k_2}[(10k_1 - 5)\cos\frac{\pi}{10} + (-5k_1 + 2)\cos\frac{\pi}{5} - 2\cos\frac{2\pi}{5} - 5k_1 + 4] \\ E = \frac{1}{5k_1}[-5k_1 - 2 + (10k_1 + 4)\cos\frac{\pi}{20} - (10k_1 + 5)\cos\frac{\pi}{10} + (10k_1 + 6)\cos\frac{3\pi}{20} - (10k_1 + 6)\cos\frac{\pi}{5} \\ \quad + (10k_1 + 6)\cos\frac{\pi}{4} - (10k_1 + 5)\cos\frac{3\pi}{10} + (10k_1 + 4)\cos\frac{7\pi}{20} - (5k_1 + 4)\cos\frac{2\pi}{5} + 4\cos\frac{9\pi}{20}] \\ F = \frac{1}{5k_2}[-5k_1 - 4 + (10k_1 + 8)\cos\frac{\pi}{20} - (10k_1 + 5)\cos\frac{\pi}{10} + (10k_1 + 2)\cos\frac{3\pi}{20} \\ \quad - (5k_1 + 2)\cos\frac{\pi}{5} + 2\cos\frac{\pi}{4} - 2\cos\frac{7\pi}{20} + 2\cos\frac{2\pi}{5} - 2\cos\frac{9\pi}{20}] \end{cases} \tag{64}$$

$$u_{\mathrm{mAn}}(\omega t) = \begin{cases} (\frac{2-5k_1}{10k_1} + \frac{4-5k_1}{10k_2})\alpha_1 - (\frac{2+5k_1}{5k_1} + \frac{4+5k_1}{5k_2})\alpha_2 \quad \omega t \in [\varphi, \varphi + \frac{\pi}{20}] \cup [\varphi + \frac{19\pi}{20}, \varphi + \pi] \\ (\frac{2-5k_1}{10k_1} + \frac{4-5k_1}{10k_2})\alpha_1 + (\frac{2+5k_1}{5k_1} + \frac{4+5k_1}{5k_2})\alpha_2 \omega t \in [\varphi + \frac{\pi}{20}, \varphi + \frac{\pi}{10}] \cup [\varphi + \frac{9\pi}{10}, \varphi + \frac{19\pi}{20}] \\ (\frac{-3+5k_1}{10k_1} + \frac{-1+5k_1}{10k_2})\alpha_1 - (\frac{3+5k_1}{5k_1} + \frac{1+5k_1}{5k_2})\alpha_2 \omega t \in [\varphi + \frac{\pi}{10}, \varphi + \frac{3\pi}{20}] \cup [\varphi + \frac{17\pi}{20}, \varphi + \frac{9\pi}{10}] \\ (\frac{-3+5k_1}{10k_1} + \frac{-1+5k_1}{10k_2})\alpha_1 + (\frac{3+5k_1}{5k_1} + \frac{1+5k_1}{5k_2})\alpha_2 \omega t \in [\varphi + \frac{3\pi}{20}, \varphi + \frac{\pi}{5}] \cup [\varphi + \frac{4\pi}{5}, \varphi + \frac{17\pi}{20}] \\ (\frac{3-5k_1}{10k_1} + \frac{1}{10k_2})\alpha_1 - (\frac{3+5k_1}{5k_1} + \frac{1}{5k_2})\alpha_2 \omega t \in [\varphi + \frac{\pi}{5}, \varphi + \frac{\pi}{4}] \cup [\varphi + \frac{3\pi}{4}, \varphi + \frac{4\pi}{5}] \\ (\frac{3-5k_1}{10k_1} + \frac{1}{10k_2})\alpha_1 + (\frac{3+5k_1}{5k_1} + \frac{1}{5k_2})\alpha_2 \omega t \in [\varphi + \frac{\pi}{4}, \varphi + \frac{3\pi}{10}] \cup [\varphi + \frac{7\pi}{10}, \varphi + \frac{3\pi}{4}] \\ (\frac{-2+5k_1}{10k_1} + \frac{1}{10k_2})\alpha_1 - (\frac{2+5k_1}{5k_1} - \frac{1}{5k_2})\alpha_2 \omega t \in [\varphi + \frac{3\pi}{10}, \varphi + \frac{7\pi}{20}] \cup [\varphi + \frac{13\pi}{20}, \varphi + \frac{7\pi}{10}] \\ (\frac{-2+5k_1}{10k_1} + \frac{1}{10k_2})\alpha_1 + (\frac{2+5k_1}{5k_1} - \frac{1}{5k_2})\alpha_2 \omega t \in [\varphi + \frac{7\pi}{20}, \varphi + \frac{4\pi}{10}] \cup [\varphi + \frac{3\pi}{5}, \varphi + \frac{13\pi}{20}] \\ (\frac{1}{5k_1} - \frac{1}{10k_2})\alpha_1 - (\frac{2}{5k_1} - \frac{1}{5k_2})\alpha_2 \omega t \in [\varphi + \frac{4\pi}{10}, \varphi + \frac{9\pi}{20}] \cup [\varphi + \frac{11\pi}{20}, \varphi + \frac{3\pi}{5}] \\ (\frac{1}{5k_1} - \frac{1}{10k_2})\alpha_1 + (\frac{2}{5k_1} - \frac{1}{5k_2})\alpha_2 \omega t \in [\varphi + \frac{9\pi}{20}, \varphi + \frac{\pi}{2}] \cup [\varphi + \frac{\pi}{2}, \varphi + \frac{11\pi}{20}] \end{cases} \tag{65}$$

$$i_{\mathrm{ja}}(\omega t) = \begin{cases} -\cos\omega t + \cos\varphi - u_{\mathrm{mAn1}}(\omega t - \varphi) + S_1 \omega t \in [\varphi, \varphi + \frac{\pi}{20}] \\ -\cos\omega t + \cos\varphi - u_{\mathrm{mAn2}}(\omega t - \varphi) + S_2 \omega t \in [\varphi + \frac{\pi}{20}, \varphi + \frac{\pi}{10}] \\ -\cos\omega t + \cos\varphi - u_{\mathrm{mAn3}}(\omega t - \varphi) + S_3 \omega t \in [\varphi + \frac{\pi}{10}, \varphi + \frac{3\pi}{20}] \\ \vdots \\ -\cos\omega t + \cos\varphi - u_{\mathrm{mAni}}(\omega t - \varphi) + S_{\mathrm{i}} \omega t \in [\varphi + \frac{(i-1)\pi}{20}, \varphi + \frac{i\pi}{20}]. \end{cases} \tag{66}$$

REFERENCES

[1] S. Kwak and H. A. Toliyat, "Current-source-rectifier topologies for sinusoidal supply current: Theoretical studies and analyses," *IEEE Trans. Ind. Electron.*, vol. 53, no. 3, pp. 984–987, Jun. 2006.

[2] J. R. Rodríguez *et al.*, "Large current rectifiers: State of the art and future trends," *IEEE Trans. Ind. Electron.*, vol. 52, no. 3, pp. 738–746, Jun. 2005.

[3] J. Chen, Y. Shen, J. Chen, H. Bai, C. Gong, and F. Wang, "Evaluation on the auto-configured multi-pulse AC/DC rectifiers and their application in more electric aircrafts," *IEEE Trans. Transp. Electrific.*, vol. 6, no. 4, pp. 1721–1739, Dec. 2020.

[4] Q. Du, L. Gao, Q. Li, T. Li, and F. Meng, "Harmonic reduction methods at DC side of parallel-connected multipulse rectifiers: A review," *IEEE Trans. Power Electron.*, vol. 36, no. 3, pp. 2768–2782, Mar. 2021.

[5] Y. Lian, S. Yang, K. Xu, Y. Li, and W. Yang, "Harmonic reduction mechanism at DC link of two different 24-pulse rectifiers," in *Proc. IEEE Transp. Electrific. Conf. Expo, Asia-Pac.*, 2017, pp. 1–6.

[6] S. Bai and S. M. Lukic, "New method to achieve AC harmonic elimination and energy storage integration for 12-pulse diode rectifiers," *IEEE Trans. Ind. Electron.*, vol. 60, no. 7, pp. 2547–2554, Jul. 2013.

[7] S. Fukuda, M. Ohta, and Y. Iwaji, "An auxiliary-supply-assisted harmonic reduction scheme for 12-pulse diode rectifiers," *IEEE Trans. Power Electron.*, vol. 23, no. 3, pp. 1270–1277, May 2008.

[8] L. Gao, X. Xu, Z. Man, and J. Lee, "A 36-pulse diode-bridge rectifier using dual passive harmonic reduction methods at DC link," *IEEE Trans. Power Electron.*, vol. 34, no. 2, pp. 1216–1226, Feb. 2019.

[9] P. S. Prakash, R. Kalpana, K. S. Chethana, and B. Singh, "A 36-pulse AC-DC converter with DC side tapped interphase bridge rectifier for power quality improvement," *IEEE Trans. Ind. Appl.*, vol. 6, no. 4, pp. 1721–1739, Dec. 2020.

[10] Y. Li, K. Xu, Y. Lian, W. Yang, and S. Yang, "A novel 36-pulse rectifier with a low loss interphase converter at DC side," in *Proc. IEEE Transp. Electrific. Conf. Expo, Asia-Pac.*, 2017, pp. 1–6.

[11] F. J. Chivite-Zabalza and A. J. Forsyth, "A simple, passive 24-pulse AC-DC converter with inherent load balancing using harmonic voltage injection," in *Proc. IEEE 36th Power Electron. Spec. Conf.*, 2005, pp. 76–82.

[12] F. J. Chivite-Zabalza, A. J. Forsyth, and D. R. Trainer, "A simple, passive 24-pulse AC–DC converter with inherent load balancing," *IEEE Trans. Power Electron.*, vol. 21, no. 2, pp. 430–439, Mar. 2006.

[13] F. J. Chivite-Zabalza and A. J. Forsyth, "A passive 36-pulse AC–DC converter with inherent load balancing using combined harmonic voltage and current injection," *IEEE Trans. Power Electron.*, vol. 22, no. 3, pp. 1027–1035, May 2007.

[14] F. J. Chivite-Zabalza, A. J. Forsyth, and I. Araujo-Vargas, "36-pulse hybrid ripple injection for high-performance aerospace rectifiers," *IEEE Trans. Ind. Appl.*, vol. 45, no. 3, pp. 992–999, May/Jun. 2009.

[15] F. J. Chivite-Zabalza and A. J. Forsyth, "A 48-pulse converter using DC-ripple injection," in *Proc. 7th Int. Conf. Power Electron. Drive Syst.*, 2007, pp. 599–606.

[16] F. Meng, Q. Du, L. Wang, L. Gao, and Z. Man, "A series-connected 24-pulse rectifier using passive voltage harmonic injection method at DC-link," *IEEE Trans. Power Electron.*, vol. 34, no. 9, pp. 8503–8512, Sep. 2019.

[17] Q. Li, F. Meng, L. Gao, H. Zhang, and Q. Du, "A 30-pulse rectifier using passive voltage harmonic injection method at DC link," *IEEE Trans. Ind. Electron.*, vol. 67, no. 11, pp. 9273–9291, Nov. 2020.

[18] S. Prakash P. R. Kalpana, B. Singh, and G. Bhuvaneswari, "A 20-pulse asymmetric multiphase staggering autoconfigured transformer for power quality improvement," *IEEE Trans. Power Electron.*, vol. 33, no. 2, pp. 917–925, Feb. 2018.

[19] B. Singh and S. Gairola, "A 40-pulse AC-DC converter fed vector-controlled induction motor drive," *IEEE Trans. Energy Convers.*, vol. 23, no. 2, pp. 403–411, Jun. 2008.

Qingxiao Du was born in Shandong, China, in 1995. She received the B.S. degree in electrical engineering from the Harbin Institute of Technology, Weihai, China, in 2017, and the M.S. degree in electrical power engineering from the University of Southampton, Southampton, U.K., in 2018. She is currently working toward the Ph.D. degree in electrical engineering with the Harbin Institute of Technology.

Her research interests include harmonic elimination and fault analysis on high-power rectifiers.

Wei Liu was born in Shandong, China, in 1997. He received the B.S. degree in electrical engineering, in 2020, from the Harbin Institute of Technology, Weihai, China, where he is currently working toward the M.S. degree in power electronics and power drives.

His research interests include power electronic transformer and power decoupling control.

Quanhui Li was born in Shandong, China, in 1996. He received the B.S. and M.S. degrees in electrical engineering, in 2018 and 2020, respectively, from the Harbin Institute of Technology, Weihai, China, where he is currently working toward the Ph.D. degree in electrical engineering.

His research interests include multipulse rectifier and high-power rectification.

Lei Gao was born in Hebei, China, in 1982. She received the B.S., M.S., and Ph.D. degrees in electrical engineering from the Harbin Institute of Technology, Harbin, China, in 2005, 2007, and 2012, respectively.

Since 2012, she has been working as an Assistant Professor with the Harbin Institute of Technology, Weihai, China. Her current research interests include power electronics and motor drives.

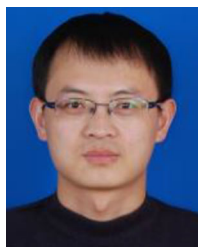

Fangang Meng (Member, IEEE) was born in Shandong, China, in 1982. He received the B.S. degree in thermal energy and power engineering, in 2005, and the M.S. and Ph.D. degrees in electrical engineering from the Harbin Institute of Technology, Harbin, China, in 2007 and 2011, respectively.

Since 2020, he has been working as a Professor with the Harbin Institute of Technology, Weihai, China. His research interests include harmonic detection, stability analysis of converter, and high-power rectification.